Generation of green second harmonic radiation in LBO, BiBO, KTP, and PPLN crystals using passively Q-switched sub-nanosecond microchip laser

by

Kostyantyn Sukhoy

A Thesis submitted to the Faculty of Graduate Studies of
The University of Manitoba
in partial fulfillment of the requirements for the degree of

Master of Science

Department of Electrical and Computer Engineering
University of Manitoba
Winnipeg, Manitoba
Canada

Author's Declaration

I hereby declare that I am the sole author of this thesis. This is not a finalized copy of my thesis. This is a nearly finalized draft of my thesis submitted to my examining committee for their consideration.

I understand that an electronic copy of the finalized draft of my thesis may be made electronically available to the public.

Abstract

A sub-nanosecond green laser source has big demand in such fields like spectroscopy, micromachining, fluorescence imaging, and laser displays. Most often green light is produced by frequency doubling of pulsed laser sources based on Nd^{3+}-ion or Yb^{3+}-ion doped gain media that oscillate in the near-IR range. For creating compact and relatively small source of green light suitable for broad type of applications a passively Q-switched Nd:YAG microchip laser (Teem Photonics) operating at 1064 nm with 6.9 kHz repetition rate was chosen. It delivers 560 ps long pulses with 10 μJ energy, corresponding to an average output power of 69 mW. Crystals of BiBO, KTP, LBO, and PPLN were chosen for frequency doubling. Main goal of this work was to study the characteristics of these crystals under similar experimental conditions and to select the most efficient one for this task. To optimize second harmonic generation (SHG) process, different focusing conditions were used during the experiments. In this work we measured the second harmonic output power as a function of the incident power, beam profile for fundamental and second harmonic radiation for all crystals, and second harmonic output power as a function of temperature for PPLN crystal. Crystal of PPLN was found to be the most suitable for SHG process and produced it with up to 60% conversion efficiency.

Acknowledgement

I would like to especially thank my supervisor Professor Arkady Major for his guidance and support from the initial to the final level this project. I owe my deepest gratitude to my colleague Haitao Zhao for help during all my staying at the University. I would like to express my sincere appreciation to Professor Ivan T. Lima Jr. for the opportunity to work with his equipment.

Lastly, I offer my regards and blessings to all of those who supported me in any respect during the completion of the project.

Contents

List of Symbols

IR- Infrared

SHG – Second harmonic generation

NLO – Nonlinear optics

OPO - Optical parametric oscillation

OPG - Optical parametric generation

OPA - Optical parametric amplification

CARS - Coherent anti-Stokes Raman scattering

STED - Stimulated emission depletion

DNA - Deoxyribonucleic acid

KTP - Potassium titanyl phosphate ($KTiOPO_4$)

BBO - Beta barium borate (β-BaB_2O_4)

KDP - Potassium dihydrogen phosphate

LBO - Lithium triborate (LiB_3O_5)

BiBO- Bismuth triborate (BiB_3O_6)

PPLN- Periodically poled lithium niobate ($LiNbO_3$)

Nd:YAG - Neodymium-doped yttrium aluminum garnet

QPM - Quasi-phase-matching

CW – Continues wave

E - Electric field

P – Polarization

ε - Dielectric constant

P_L -Linear polarization

P_{NL} -Nonlinear polarization

$\chi^{(1)}$- Linear susceptibility

$\chi^{(2)}$- Nonlinear susceptibility

d - Nonlinear coefficient

d_{eff} - Effective nonlinear coefficient

k - Wave vector

μ_0 - Vacuum permeability

ω - Frequency

n - Index of refraction

λ – Wavelength

h – Dimensionless coefficient

$\hbar$ – Plank's constant

Θ - Phase-matching angle

φ - Azimuth angle

l_c - Coherence length

$\boldsymbol{r}$ - Walk-off angle

l_a – Aperture length

w - Radius of the beam

A - Effective area

Is - Input intensity

I_{SHG} – SHG intensity

Lc – Crystal length

η - SHG efficiency

$\Delta\Theta$ – Angular acceptance

$\Delta\lambda$ – Spectral acceptance

T – Temperature

ΔT – Temperature acceptance

List of Figures

List of Tables

Introduction

Pulsed sources of green radiation based on diode-pumped microchip lasers [1-4] are attractive for many industrial, scientific and medical applications, where one or more of the following features are required: sub-nanosecond pulse width, high peak power, high repetition rate, structural compactness and low cost. In particular, such laser systems exhibit great potential and demonstrate their value for biomedical applications such as CARS (Coherent Anti-Stokes Raman Scattering) spectroscopy [5], supercontinuum generation [6], STED (Stimulated Emission Depletion) microscopy [7], fluorescence lifetime imaging microscopy [8], protein micro fabrication [9], and optical DNA biosensors [10]. Passively Q-switched sub-nanosecond microchip lasers are well suited for these purpose as they combine high efficiency, reliability, low cost, size, and complexity [8-12]. A combination of pulsed microchip laser with highly nonlinear material for second harmonic generation offers a simple and effective way to produce pulsed visible radiation. One of the challenges that push forward the development of such systems is the enhancement of the conversion efficiency. The conventional green microchip lasers based on KTP, BBO, KDP or LBO crystals have relatively low efficiency limited by their low nonlinear coefficients, spatial walk-off effect and inconvenient matching angle. Although 70% conversion efficiency was reported based on KTP crystal [1], most of the results are in the range between 25% and 55% [11-14]. Therefore our motivation was to explore relatively new crystals of BiBO and PPLN which have the potential to serve as efficient frequency doublers of a Q-switched microchip laser to produce a compact and reliable source of green radiation.

The BiB_3O_6 (bismuth triborate, BiBO) crystal was introduced by Hellwig *et al.* in 1998. Its effective second-order nonlinearity was determined to be 3.2 pm/V at 1079 nm and is larger than that for the well-known BBO, KDP, and LBO crystals [15]. Because it also has a transparency range of 280-2500 nm, BiBO is an excellent nonlinear material for frequency conversion into the visible and ultraviolet wavelength ranges. These attractive properties have been recently exploited to demonstrate the potential of BiBO for efficient second harmonic generation (SHG) using continuous-wave [16,17], long-pulse nanosecond [18,19], picosecond [20,21], and femtosecond lasers [22,23]. For example, conversion efficiencies of second harmonic generation in the pulsed regimes ranged from 11% for nanosecond pulses [18] to 68% for picoseconds pulses [20]. This crystal used critical phase-matching technique for generation of SHG.

On the other hand noncritical phase-matching or Quasi-phase-matching (QPM) technique opened a new window for enhancing the conversion efficiency, since the noncritical interaction allows one to access the much larger nonlinear coefficients of the crystal. Among several available QPM crystals such as periodically poled $LiNbO_3$ (PPLN) [24,25], periodically poled stoichiometric $LiTaO_3$ (PPSLT) [26] and periodically poled $KTiOPO_4$ (PPKTP) [27,28], the first one has the highest nonlinearity ($d_{eff} \approx 17$ pm/V), indicating its better SHG conversion ability. However PPLN has some drawbacks: for instance the low threshold of photorefractive damage at room temperature and green-induced infrared absorption greatly limit its efficiency and convenience. An improved version, MgO-doped periodically poled $LiNbO_3$ (MgO:PPLN), created in recent years is a solution to overcome these drawbacks.

Recently, most of the groups focused on the continuous wave (CW) green light generation by using MgO:PPLN crystal, but the results seem contradictory to the capacity of the crystal itself. For example, N. Pavel reported 1.18 W green light delivered from 7 W CW Nd:$GdVO_4$ laser,

corresponding to 16.8% conversion efficiency [29]. T. Suzudo reported conversion efficiency of 36% and 34% of MgO:PPLN crystal from diode-pumped Nd:$GdVO_4$ microchip laser operated in cw and quasi-cw regime respectively [30]. The highest conversion efficiency is more than 52% from an intracavity frequency doubled CW Nd:YVO_4 laser reported by M. Zhou [31]. Although advantages of this crystal are clear, only few reports were concentrated on the SHG of MgO:PPLN in Q-switched regime that produced long pulses of several hundreds of nanoseconds [32]. Therefore, the regime of SHG with sub-nanosecond pulses was not yet explored with MgO:PPLN and was one of the tasks of this work.

2. Theory of Frequency Doubling

Nonlinear optics is a section of optics that covers the study of propagation of powerful light beams in the solids, liquids and gases and their interaction with matter. Strong light field changes optical properties of the medium (such as refractive index) which become nonlinear functions of the electric field $\boldsymbol{E}$ of the light wave (e.g. $\boldsymbol{E}^2$), i.e. the induced polarization $\boldsymbol{P}$ becomes nonlinearly dependent on the electric field $\boldsymbol{E}$.

2.1 Second Harmonic Generation (SHG)

Second harmonic generation (SHG) or frequency doubling is a special case of sum frequency generation when the two input wavelengths are the same. History of nonlinear optical devices based on second harmonic generation started their way in 1961, when Franken *et. al.* detected this effect using a ruby laser and quartz crystal [33]. Since this day frequency doubling, which utilizes nonlinear optical response in intense coherent radiation beam, has been widely used for frequency conversion of various lasers. Nonlinear optical effects mainly arise from a distortion of the electron clouds around the atoms in the material as they interact with electric field $\boldsymbol{E}$ of a light wave (Figure 2.1).

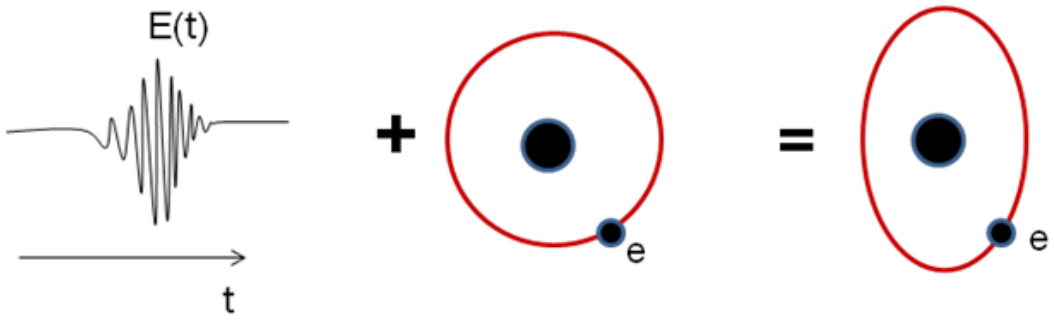

Figure 2.1: Interaction of intense radiation with atom.

This distortion is changing the dielectric constant ε which results in induced polarization of matter. Nonlinear effect is relatively small and can be seen only in strong radiation field. Total polarization can be written as:

$$\mathbf{P}=\mathbf{P_L}+\mathbf{P_{NL}}\ , \tag{2.1}$$

where $\mathbf{P_L}$ -is linear polarization and $\mathbf{P_{NL}}$ –is nonlinear polarization. We can express the magnitude of the induced polarization per unit volume **P** as a series of powers of magnitude of the applied electric field **E**

$$\mathbf{P} = \varepsilon_0\chi^{(1)}\mathbf{E} + \varepsilon_0\chi^{(2)}\mathbf{EE} + \varepsilon_0\chi^{(3)}\mathbf{EEE} + \cdot\cdot, \tag{2.2}$$

where ε_0 is permittivity of free space or dielectric constant ($8.854187817...\times10^{-12}$ F/m) , and $\chi^{(1)}$-is the linear susceptibility representing the linear response of the material; $\chi^{(2)}$ is the nonlinear susceptibility representing the second order of nonlinear response of the material; $\chi^{(3)}$ is the nonlinear susceptibility representing the third order of nonlinear response of the material. The linear optical susceptibility $\chi^{(1)}$ is a constant dielectric response of medium. For the second order nonlinear effect, we will consider $\chi^{(2)}$ which is a tensor with 27 elements. However, the number of independent components of $\chi^{(2)}$ is much smaller [34]. The effects based on $\chi^{(2)}$ can be seen only in anisotropic media such as crystals. Typically $\chi^{(1)} >> \chi^{(2)} >> \chi^{(3)}$ and thus the nonlinear effect is very small and could be negligible at normal circumstances as shown on Figure 2.2.

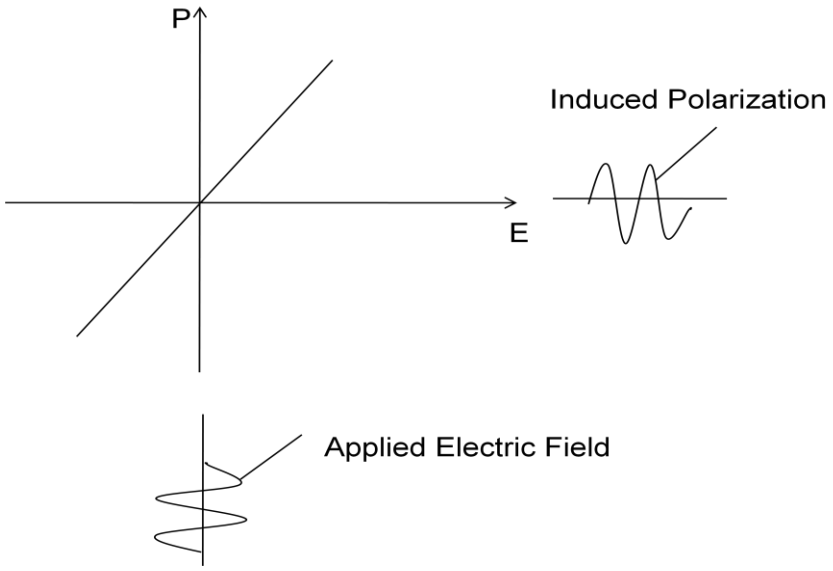

Figure 2.2: A medium in which the induced polarization is a linear function of the applied electric field [34].

Therefore we can see the generation of nonlinear polarization (i.e. distorted response) only when we apply intense light to nonlinear media. In this case $\chi^{(2)}$ is the nonlinear susceptibility representing the second order of nonlinear response of the material. As shown in Figure 2.3, the induced polarization also has a nonlinear component ($2\omega_i$) at twice the frequency of the applied field [34].

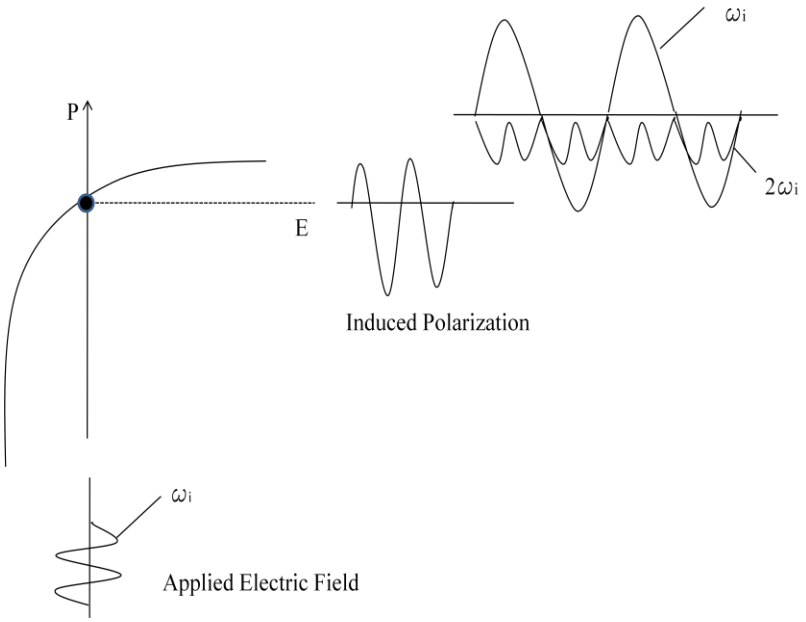

Figure 2.3: A medium in which the induced polarization is a nonlinear function of the applied electric field [34].

The electric field strength of a monochromatic laser beam can be written as

$$\mathbf{E} = E(t)e^{-i\omega t} + c.c. \,, \tag{2.3}$$

where ***c.c.*** denotes complex conjugate. Substituting this expression into equation (2.2) yields for the second order polarization:

$$\mathbf{P}^{(2)} = \chi^{(2)}(E^2 e^{-2i\omega t} + c.c.) + 2\,\chi^{(2)} EE^*, \tag{2.4}$$

This equation shows that in a medium for which the second order susceptibility is nonzero, the created nonlinear polarization contains a contribution of the frequency ***2ω***. Therefore, the electromagnetic radiation generated by the polarization wave contains a contribution at the second harmonic (SH) frequency of the incident laser beam [35]. So far we described only the effect of SHG, however higher orders of susceptibilities can generate other frequencies, e.g. third harmonic.

Rather than using susceptibility tensor $\chi^{(2)}$ itself, it is more common for technical literature to use ***"nonlinear coefficient"*** parameter ***d.*** Considering intrinsic permutation symmetry, the last two subscripts of the ***d*** tensor (***jk)*** can be contracted to single index ***l*** according to the following Table 2.1. For example, $d_{xyz} = d_{xzy} = d_{il} = d_{31}$

Table 2.1: Replacement of indices *jk* by a single index *l* [37].

I	***jk***	***Jk***	***L***
X 1	XX	11	1
Y 2	YY	22	2
Z 3	ZZ	33	3
	YZ=ZY	23,32	4
	XZ=ZX	31,13	5
	XY=YX	12,21	6

Here the nonlinear coefficient ***d*** we can express like

$$d_{il} = 1/2\ \chi^{(2)}_{ijk} \tag{2.5}$$

where ***i, j ,k*** – directions in a space indexing $\chi^{(2)}_{ijk}$. And polarization equation (2.2) we can express like:

$$P_i(E) = 2d_{ijk} E_j E_k \tag{2.6}$$

If we apply this approach, this replacement reduces the nonlinear susceptibility tensor to a 3x6 matrix.

$$\boldsymbol{P_i(E) = 2}\begin{bmatrix} \boldsymbol{d_{11}} & \boldsymbol{d_{12}} & \boldsymbol{d_{13}} & \boldsymbol{d_{14}} & \boldsymbol{d_{15}} & \boldsymbol{d_{16}} \\ \boldsymbol{d_{21}} & \boldsymbol{d_{22}} & \boldsymbol{d_{23}} & \boldsymbol{d_{24}} & \boldsymbol{d_{25}} & \boldsymbol{d_{26}} \\ \boldsymbol{d_{31}} & \boldsymbol{d_{32}} & \boldsymbol{d_{33}} & \boldsymbol{d_{34}} & \boldsymbol{d_{35}} & \boldsymbol{d_{36}} \end{bmatrix} \begin{pmatrix} \boldsymbol{E_{1,x}E_{2,x}} \\ \boldsymbol{E_{1,y}E_{2,y}} \\ \boldsymbol{E_{1,z}E_{2,z}} \\ \boldsymbol{E_{1,y}E_{2,z} + E_{2,y}E_{1,z}} \\ \boldsymbol{E_{1,x}E_{2,z} + E_{2,x}E_{1,z}} \\ \boldsymbol{E_{1,x}E_{2,y} + E_{2,x}E_{1,y}} \end{pmatrix} \tag{2.7}$$

For frequency doubling this simplification is always valid, taking into account that two of the involved frequencies are the same. More detailed information can be found in [34,37].

The effective nonlinearities for SHG of 1064 nm radiation, determined for the different phase matching directions from the efficiency measured for single pass SHG, can be calculated with the following equation assuming a diffraction limited beam propagation [36]:

$$\boldsymbol{d_{eff}} = \sqrt{\frac{\boldsymbol{n(\omega)^2\, n(\omega)\pi}}{\boldsymbol{2\mu_0^{\frac{3}{2}}\varepsilon_0^{\frac{1}{2}}\omega^2}} \frac{\boldsymbol{\frac{P_{2\omega}}{P_\omega^2}}}{\boldsymbol{lk_\omega\, h}}} \tag{2.8}$$

where $\boldsymbol{P_\omega}$ is the fundamental power inside the crystal, $\boldsymbol{P_{2\omega}}$ is the power of the second harmonic, $\boldsymbol{k_\omega}$ is the wave vector of the fundamental, $\boldsymbol{\varepsilon_0}$ is the dielectric constant, $\boldsymbol{\mu_0}$ is the vacuum permeability, $\boldsymbol{l}$ is the length of the crystal and $\boldsymbol{n}$ is the refractive index. The quantity $\boldsymbol{h}$ is a dimensionless coefficient which depends on the birefringence of the crystal and the focusing conditions.

2.2 Birefringent Phase Matching

The phase matching of the fundamental and harmonic waves for second harmonic generation was independently showed by Giordmaine (1962) and Maker *et al.* (1952) [37]. In the crystal the

propagating fundamental wave has the index of refraction n_w. The produced SHG wave propagates independently at a velocity determined by the refractive index n_{2w} . Due to dispersion of the nonlinear crystal, n_w is different from n_{2w} and the fundamental and second harmonic waves propagate with individual velocities. Interference of these waves could be destructive or constructive and depends on relative phase. Coherence length ***lc*** is the propagation distance after which the two waves will have a phase difference of π.

$$lc = (\lambda_w)/(4(n_{2w} - n_w)), \tag{2.9}$$

According to this periodic power flow, the second harmonic wave reaches an intensity maximum at ***lc*** behind the front end of the crystal. Full-cycle period lengths for visible and near infrared light are in the range of a few micrometers to tens of micrometers.

The frequencies and wave vectors of the three waves are governed by the following equations

$$\omega_3 = \omega_1 + \omega_2 , \tag{2.10}$$

where ω_3 - second harmonic frequencies, ω_1, ω_2- fundamental frequencies, for SHG $\omega_1 = \omega_2$.

Conservation of momentum states that

$$\hbar k(2\omega) = \hbar k(\omega) + \hbar k(\omega) - \Delta k, \tag{2.11}$$

where $\hbar$ is the Plank's constant. Phase matching is achieved whenever $\Delta k = 0$

$$\hbar k(2\omega) = \hbar k(\omega) + \hbar k(\omega), \tag{2.12}$$

where

$$k(\omega) = \frac{2\pi}{\lambda} n(\omega) , \tag{2.13}$$

and

$$k(2\omega) = \frac{2\pi}{\frac{\lambda}{2}} n(2\omega), \tag{2.14}$$

Substituting (2.13) and (2.14) into (2.12) we will have

$$\frac{4\pi}{\lambda}n(2\omega)=\frac{4\pi}{\lambda}n(\omega), \tag{2.15}$$

and finally

$$n(2\omega) = n(\omega), \tag{2.16}$$

This means that we should find such direction of propagation of light in the crystal, where the refraction index $n(\omega)$ for incident light equals the refraction index for second harmonic $n(2\omega)$. In this case both waves travel together and efficient energy conversion is possible. On the Figure 2.4 we can see it graphically. This situation is impossible in isotropic media, since in such media refractive index n is increasing along with frequencyω. However, this condition can be satisfied in birefringent (i.e. anisotropic) crystals.

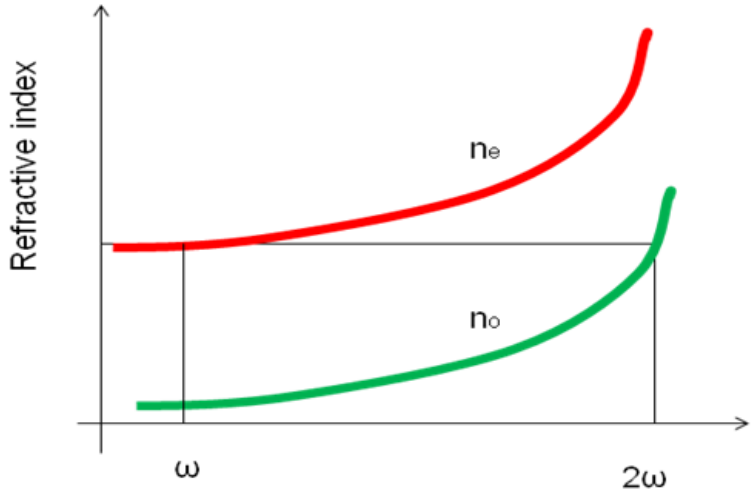

Figure 2.4: Phase matching condition in anisotropic crystal.

This type of phase matching is called birefringent or index phase matching. As we already mentioned above, in anisotropic crystals the refractive index depends on incident field polarization and direction of propagation. The optical axis for this type of crystals is defined as

direction where refractive index doesn't change in case of changing polarization of light [33]. Anisotropic crystals could have one or two optical axes.

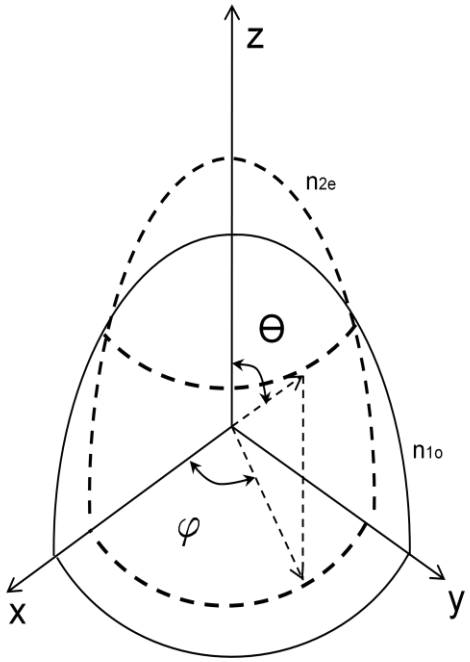

Figure 2.5: Wave surfaces of a negative uniaxial crystal. Where full lines, wave surfaces at second harmonic frequency; broken lines, wave surfaces at fundamental frequency; **Θ** is the phase-matching angle measured from the optical axis z; φ is the azimuth angle measured from x [33].

The refractive index varies with the orientation of the polarization with respect to optical axis. If the polarization is perpendicular to the optical axis, it is known as ordinary polarization. Parallel polarization is known as extraordinary. This is shown schematically in Figure 2.5. Two types of phase matching in birefringent crystals are possible in principle. **Type I**: both input waves have the same polarization while an output wave has orthogonal polarization as shown in Figure 2.6.

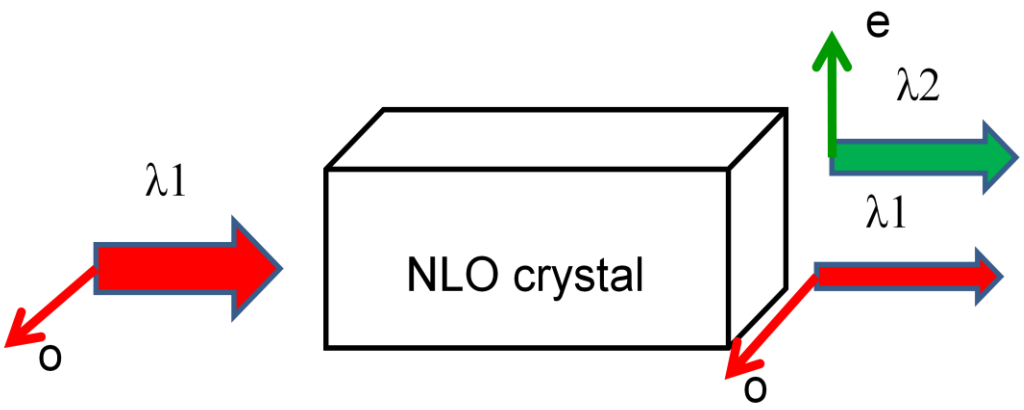

Figure 2.6: Type I phase matching.

Type II: when one wave is an extraordinary ray, the other is an ordinary ray, and the output SH wave could be ordinary or extraordinary (depending on type of birefringence in a crystal). This situation is shown in Figure 2.7.

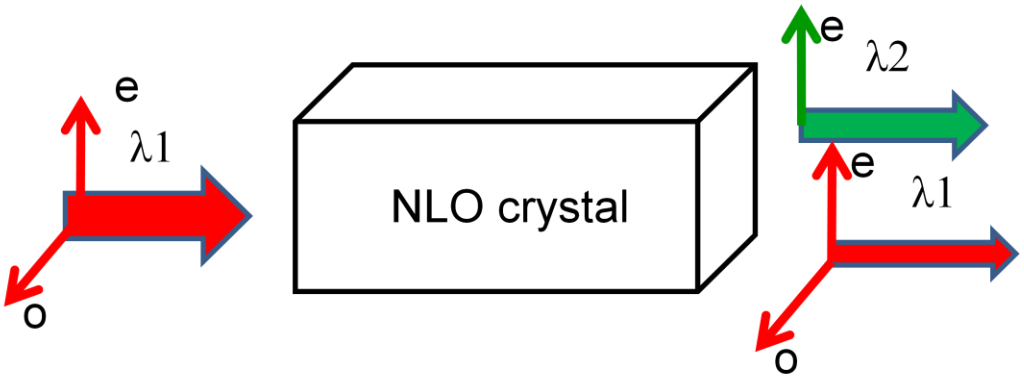

Figure 2.7: Type II of phase matching.

In type I full birefringence is used, and in type II only half of it. Figures 2.6 and 2.7 have been provided to help you visualize the polarization properties in second harmonic generation.

The refractive indices of the two waves which can propagate in a crystal at an angle $\boldsymbol{\Theta}$ to the optic axis are given by the following equation:

$$\boldsymbol{n_e(\Theta) = \frac{n_o n_e}{\sqrt{n_o^2 sin^2(\Theta) + n_e^2 cos^2(\Theta)}}} \quad (2.17)$$

where ***no*** is the ordinary refractive index of crystal, ***ne*** is the extraordinary refractive index of crystal. Usually nonlinear optical (NLO) crystals are cut normal to $\boldsymbol{\Theta}$ to match the required orientation. In this case such crystal needs to be rotated around one axis. Because of relatively sensitive angular alignment this technique is called critical phase matching. In case of $\boldsymbol{\Theta = 90^0}$, refractive indices of both waves are almost equal and we can achieve phase matching by temperature tuning (index of refraction is a function of temperature). This type of phase matching is called noncritical. It has an advantage of spatial walk-off due to birefringence being equal to zero. As a result we can focus incident light into the crystal more tightly. Major drawback of this method is the need to maintain the crystal's temperature within specified limits which are usually higher than room temperature. Birefringent phase matching can be achieved when refractive indices for SH and fundamental waves are equal as we can see on Figure 2.4. Or we can say when nonlinear media compensate difference in refractive indices between fundamental and second harmonic waves [33,38].

2.3 Quasi-Phase Matching

Quasi-phasematching (QPM) was devised by Bloembergen ***et al.*** [39]. Periodically poled nonlinear crystals with quasi-phase-matching allow the generation of SHG in an efficient and broadly tunable format. These crystals can work with any type of polarization of interacting

waves. Quasi-phase-matched materials allow us to reach efficient nonlinear frequency conversion. This method is based on changing of the nonlinearity through artificial structuring of the nonlinear material.

The quasi-phase-matching in SHG is exhibited in the space domain and the wave vector mismatch domain $\Delta\boldsymbol{k}$. In the QPM method, the $\Delta\boldsymbol{k}$ can be expressed by:

$$\Delta\boldsymbol{k} = \boldsymbol{k_{2\omega}} - \mathbf{2}\boldsymbol{k_{\omega}} - \frac{\mathbf{2}\boldsymbol{\pi}}{\boldsymbol{\Lambda}}, \tag{2.18}$$

Or for $\Delta\boldsymbol{k} = \mathbf{0}$,

$$\frac{\boldsymbol{n_{2\omega}}}{\boldsymbol{\lambda_{2\omega}}} - \mathbf{2}\frac{\boldsymbol{n_{\omega}}}{\boldsymbol{\lambda_{\omega}}} - \frac{\mathbf{1}}{\boldsymbol{\Lambda}} = \mathbf{0} \tag{2.19}$$

where $\boldsymbol{\Lambda}$ is grating period of the crystal. A wide range of spectrum can be covered using grating period tuning and temperature tuning. As was mentioned earlier, distance over which a relative phase between the two waves shifts by $\boldsymbol{\pi}$ is called a coherence length (see equation 2.9). This is also the half period of the growth and decay cycle of the second harmonic. When $\Delta\boldsymbol{k} \neq \mathbf{0}$ sign of power flow from one wave to the other is dictated by the relative phase between the interacting waves. As a result, the continuous phase slip between these waves caused by their differing phase velocities leads to an alternation in the direction of the flow of power, as shown by curve C (Figure 2.8). In the ideal case ($\Delta\boldsymbol{k} = \mathbf{0}$) the second-harmonic field grows linearly with distance in the medium, and as result the intensity grows quadratically, as shown by curve A in Figure 2.8.

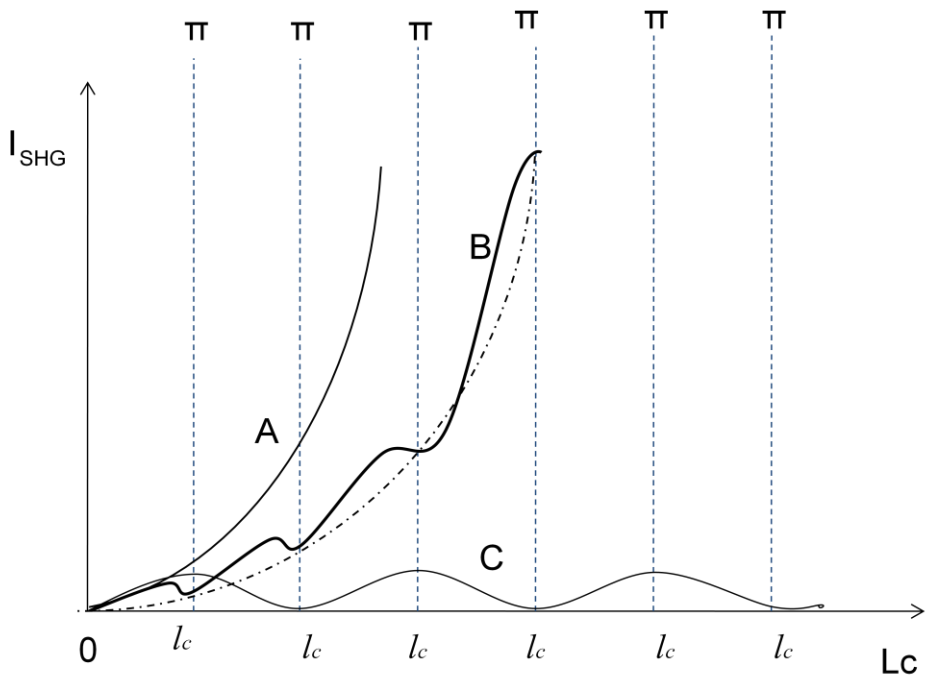

Figure 2.8: Stepwise build up of second harmonic power due to QPM. Curve A shows perfect phasematching with $\Delta k=0$; Curve B shows QPM with $\Delta k\neq 0$; Curve C shows phasematching where $\Delta k\neq 0$ [40].

QPM comprises repeated inversion of the relative phase between the incident and second harmonic waves after an odd number of coherence lengths. The phase is changing periodically so that on average, the proper phase relationship is maintained for growth of the second harmonic, as shown by curve B (Figure 2.8). One way to invert the phase is to change the sign of the nonlinear coefficient as shown in Figure 2.9. This changing could be done by two techniques. First, changing the sign of nonlinear coefficient by forming a stack of thin plates of nonlinear crystals with thickness ***lc*** which are rotated by 180^0 degrees with respect to each other.

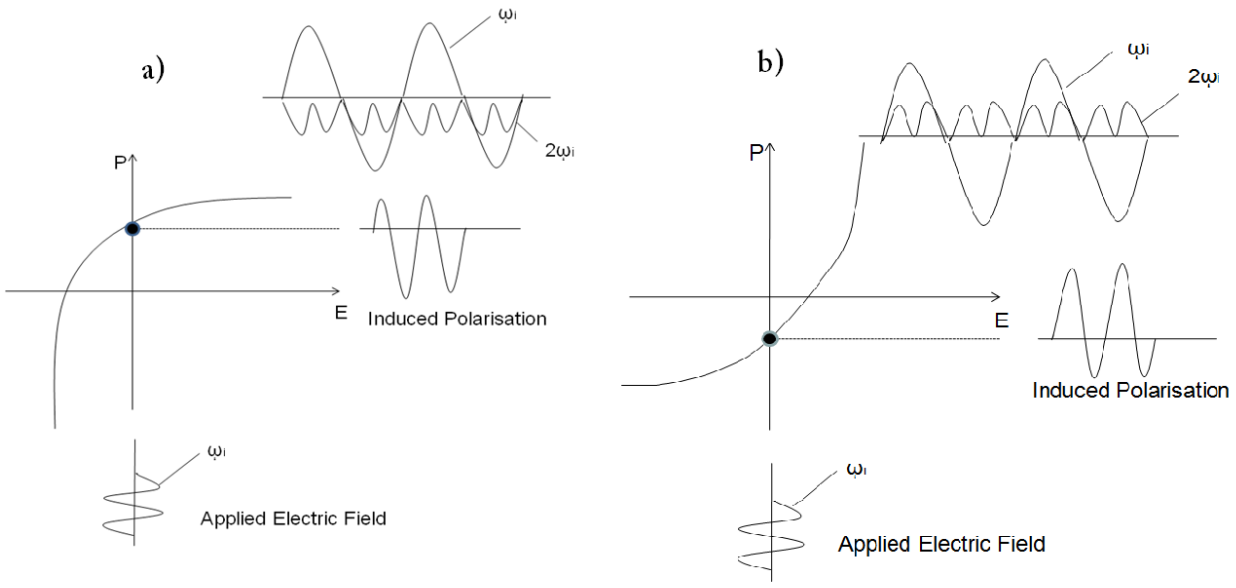

Figure 2.9: Inversion of the spontaneous polarization from a) to b) leads to a π phase shift in the generated second harmonic [34].

The second, more common way to produce it, is by using ferroelectric crystals where we can form this periodic structure by applying a strong electric field across the material [34, 40]. This process is called "poling" and such materials are called periodically poled. This is schematically presented in Figure 2.10.

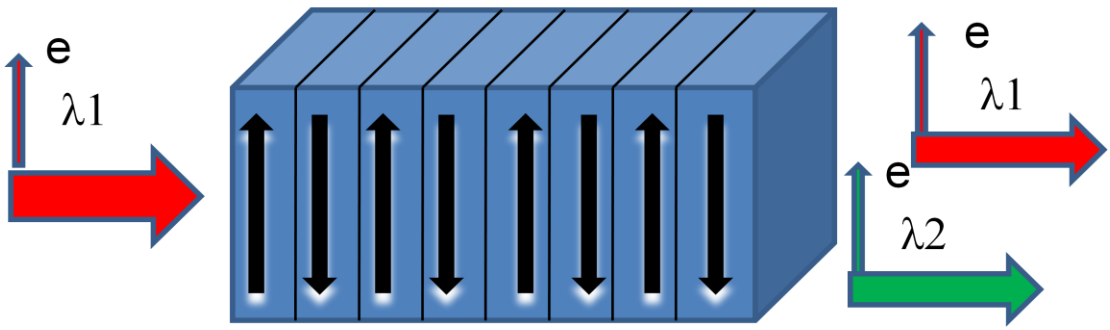

Figure 2.10: Structure of periodically poled crystal.

As follows, in periodically poled materials, birefringence is no longer needed to obtain phase matching and materials can be engineered to use their most favorable nonlinear optical coefficient which is dependent on the orientation of the crystallographic axes relative to the propagation direction of the beams.

2.4 Angle Tuning of Birefringent Phase-Matching Condition

Since index of refraction in anisotropic crystals depends on propagation direction, crystal (or angle) tilting is normally used to achieve birefringent phase-matching condition. Light polarised perpendicular to the plane containing the propagation vector $\boldsymbol{k}$ and the optical axis is said to have ordinary polarisation and for this direction $\boldsymbol{n_o}$ refractive index is called the ordinary refractive index. Light polarised in the plane containing $\boldsymbol{k}$ and the optic axis is said to have extraordinary polarisation and experiences a refractive index $\boldsymbol{n_e(\Theta)}$ that depends on the angle $\boldsymbol{\Theta}$ between the optic axis and $\boldsymbol{k}$ according to the equation [34]:

$$\boldsymbol{cos^2\,\theta = \frac{\frac{1}{n_\theta^2}-\frac{1}{n_a^2}}{\frac{1}{n_b^2}-\frac{1}{n_a^2}}}, \tag{2.20}$$

where $\boldsymbol{n_a}$ refractive index when $\boldsymbol{\Theta=0}$ and $\boldsymbol{n_b}$ refractive index when $\boldsymbol{\Theta=90^{\,o}}$ [34]. There are two axis for tilting crystal angles as is shown in Figure 2.11.

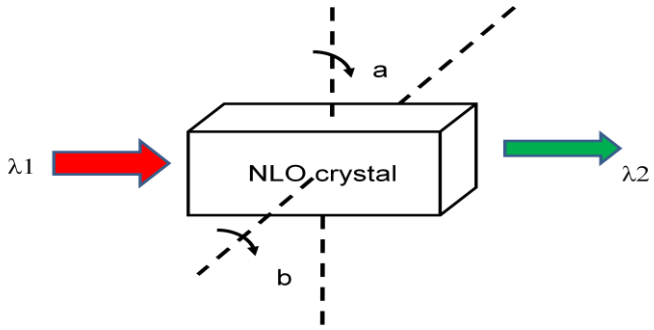

Figure 2.11: Crystal angle tilting.

Since the NLO crystals are normally cut in the principal crystal plane, conversion efficiency is not sensitive to the angle tilting around b-axis. To reach the best conversion efficiency, the crystals should be rotated just around the a-axis.

2.5 Spatial Walk-Off

Due to the birefringence of the NLO crystals, the beam of the input laser will separate from the generated beam at a walk-off angle ***r*** as shown in Figure 2.12. Therefore, the spatial walk-off limits the total length of the crystal as well as reduces the beam quality and conversion efficiency.

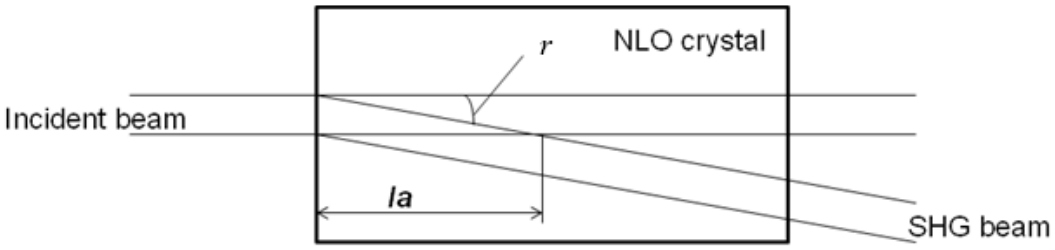

Figure 2.12: Illustration of the walk-off effect.

The beams will separate or walk off after a distance ***la*** called "aperture length" with walk off angle ***r*** [41]. The aperture length ***la*** can be calculated from the equation

$$\boldsymbol{la} = \frac{\boldsymbol{w}}{\boldsymbol{r}}\sqrt{\boldsymbol{\pi}}\ , \tag{2.21}$$

where ***w*** is a radius of the beam (μm) and ***r*** is the walk-off angle (mrad) [41].

2.6 Second Harmonic Intensity

One of the most important tasks in SHG is to obtain high conversion efficiency. We know that intensity is the Power (**P**) per unit Area (**A**) [41]:

$$\boldsymbol{I} = \frac{\boldsymbol{P}}{\boldsymbol{A}}\ , \tag{2.22}$$

$$\boldsymbol{A} = \frac{\boldsymbol{\pi}\, \boldsymbol{w_0^2}}{\boldsymbol{2}}\ , \tag{2.23}$$

where $\boldsymbol{w_0}$ is a radius of the beam and ***A*** is effective aria of the beam cross section.

The output intensity $\boldsymbol{I_{SHG}}$ has the following dependence on the effective nonlinear coefficient $\boldsymbol{d_{eff}}$, the crystal length ***Lc***, the input intensity ***Is*** and phase mismatching $\Delta\boldsymbol{k}$ [34]:

$$\boldsymbol{I_{SHG}} = \boldsymbol{d_{eff}} \boldsymbol{LcIs^2 sinc^2}\left(\frac{\boldsymbol{\Delta kLc}}{\boldsymbol{2}}\right), \tag{2.24}$$

When $\Delta\boldsymbol{k} = \boldsymbol{0}$ the refractive indices of incident fundamental and second harmonic waves are equal, and the intensity of SHG process is maximal. The characteristic dependence of SHG intensity on phase mismatch is illustrated in Figure 2.13.

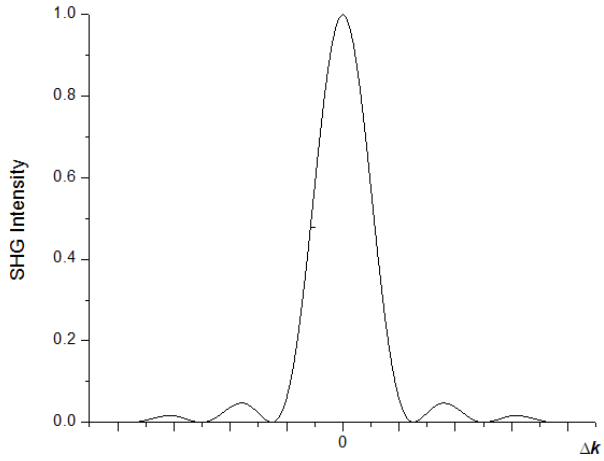

Figure 2.13: Second harmonic output intensity vs Δk.

Equation (2.24) shows that higher input intensity, longer crystal length, larger nonlinear coefficients and smaller phase mismatching will result in higher SH output and in higher conversion efficiency. Therefore the SHG efficiency $\boldsymbol{\eta}$ can be defined as:

$$\boldsymbol{\eta} = \frac{\boldsymbol{P_{2\omega}}}{\boldsymbol{P_{\omega}}} = \frac{\boldsymbol{I_{SHG}}}{\boldsymbol{I_s}} = \boldsymbol{d_{eff} L c I_s sinc^2}\left(\frac{\boldsymbol{\Delta k L c}}{\boldsymbol{2}}\right), \tag{2.25}$$

where $\boldsymbol{P_{2\omega}}$ is the SH output power and $\boldsymbol{P_{\omega}}$ is the incident beam power [34].

2.7 Angular, Spectral and Temperature Acceptances of the Crystal

Since the refractive index of anisotropic materials (in our case crystals) depends on temperature, wavelength of light and direction of propagation, the phase mismatch Δk will be a function of these parameters:

$$\Delta \boldsymbol{k} = \frac{\partial \Delta \boldsymbol{k}}{\partial \boldsymbol{T}} + \frac{\partial \Delta \boldsymbol{k}}{\partial \boldsymbol{\theta}} + \frac{\partial \Delta \boldsymbol{k}}{\partial \boldsymbol{\lambda}}, \tag{2.26}$$

where $\boldsymbol{T}$ is the temperature, $\boldsymbol{\theta}$ is the phasematching angle and $\boldsymbol{\lambda}$ is the input wavelength. As a result limits to the length of the NLO crystals and focusing conditions are restricted by angular, spectral and temperature acceptances.

2.7.1 Angular Acceptance

The angular acceptance angle or angle tolerance $\Delta\boldsymbol{\theta}$ can be defined as full angle at half maximum (FAHM), where $\boldsymbol{\theta = 0}$ is the phase-matching direction (Figure 2.14). For example, the acceptance angle of KTP for frequency doubling of Nd:YAG at 1064 nm is about 20 (mrad*cm), while BiBO has only 2.1 (mrad*cm) [45].

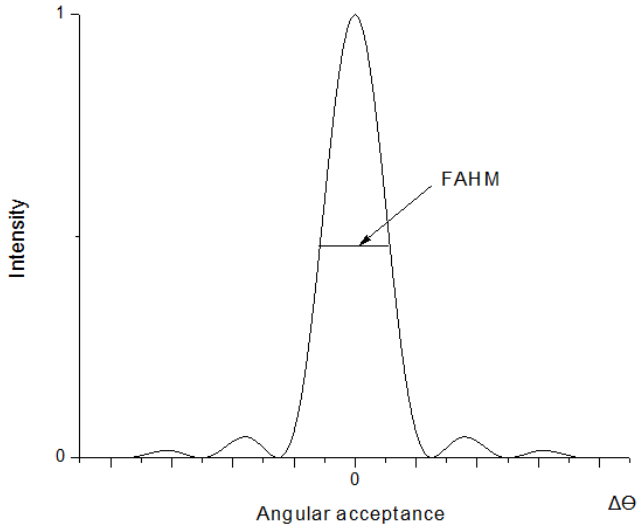

Figure 2.14: The angular acceptance (ΔΘ), full angle at half maximum (FAHM).

The angular acceptance angle $\Delta\boldsymbol{\theta}$ depends on input wavelength, length of crystal and direction of incident beam. According to [34]:

$$\Delta\boldsymbol{\theta} = \sqrt{\frac{\mathbf{1.39}\boldsymbol{\lambda}}{\boldsymbol{\pi}\left|\frac{\boldsymbol{\partial^2 n_\theta}}{\boldsymbol{\partial\theta^2}}\right|_{\boldsymbol{\theta=0}}\boldsymbol{l}}}, \tag{2.27}$$

where $\boldsymbol{l}$ is the crystal length, $\boldsymbol{n}$ is the refractive index and $\boldsymbol{\lambda}$ is the input wavelength. More generally, as can be seen from Eq. (2.24), SH output intensity has a sinc^2-type dependence on phasematching angle as shown in Figure 2.14.

2.7.2 Spectral Acceptance

Output radiation from typical lasers is usually spread over a finite range of wavelengths (or corresponding frequencies) around a center wavelength $\boldsymbol{\lambda_0}$. The spectral acceptance or phase-matching bandwidth can be defined as a frequency (or wavelength) range where the refractive indices of the pump and SH waves are equal (Figure 2.15).

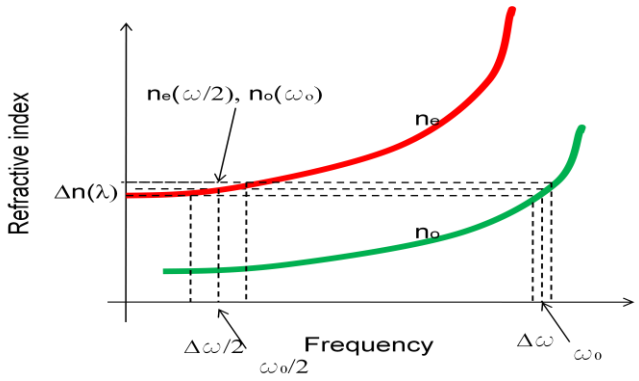

Figure 2.15: Phase-matching bandwidth in SHG.

Spectral acceptance inversely depends on the length of a crystal. The longer the crystal, the smaller the spectral acceptance. According to F.J. Kontour *et al.* [42] SH power $P_{\lambda/2}$ is equal to:

$$\boldsymbol{P_{\frac{\lambda}{2}} = P_{\lambda} sinc^2 \left[0.8858\pi \left(\frac{\lambda-\lambda_0}{\Delta\lambda_{crystal}}\right)\right]}, \tag{2.28}$$

where $\boldsymbol{\Delta\lambda_{crystal}}$ is bandwidth of the crystal is equal:

$$\boldsymbol{\Delta\lambda_{crystal} = \frac{0.4429\lambda_{\omega}}{L}\left|\frac{n_{2\omega}-n_{\omega}}{\lambda_{\omega}} + \frac{\partial n_{\omega}}{\partial\lambda} - \frac{1}{2}\frac{\partial n_{2\omega}}{\partial\lambda}\right|^{-1}}, \tag{2.29}$$

where L is length of the crystal. This equation is valid for single frequency laser radiation [34,42].

2.7.3 Temperature Acceptance

Temperature acceptance is also a very important parameter. The refractive index slightly depends on the temperature and thus it can affect $\Delta\boldsymbol{k}$. This will also result in $sinc^2$ like behavior of SH output with varying temperature. Moreover, crystal length $\boldsymbol{L}$ is also changeable as a result of thermal expansion. Temperature tuning bandwidth $\Delta\boldsymbol{T_{FWHM}}$ can be evaluated using the following equation:

$$\boldsymbol{\Delta T_{FWHM} = \left|\frac{1.39\lambda_{\omega}}{\pi L\left[\frac{\partial n_c(\lambda_{2\omega})}{\partial T} - \frac{\partial n_b(\lambda_{\omega})}{\partial T}\right]}\right|}, \tag{2.30}$$

where $\boldsymbol{\lambda_{\omega}, n_b}$ and $\boldsymbol{\lambda_{2\omega}, n_c}$ are the wavelengths and the refractive indices of the fundamental and SH radiation respectively [34].

Summary

This chapter reviewed the principles of nonlinear optics. It has emphasized ideas of second harmonic generation by birefringent and quasi-phase-matching techniques. The angle, temperature and wavelength acceptance were also discussed.

3. Materials for Second Harmonic Generation

In this section we will review nonlinear crystals that were used in our project for the design of the compact green laser. We will discuss nonlinear crystals that have been used widely as well as new materials which can have good potential for this type of work. For each material an overview of the ways it has been used and a summary of its characteristics will be provided.

3.1 Lithium Triborate (LBO) Crystal

Lithium triborate or LBO (LiB_3O_5) is one of the most popular crystals especially for high-average-power SHG owing to:

- Broad transparency range from 160nm to 2600nm,
- Broad SHG range from 550nm to 2600nm.
- Wide acceptance angle and small spatial walk-off.
- High damage threshold.
- Excellent crystal for SHG of ultra short pulsed lasers, due to its high damage threshold and small group velocity dispersion.
- High optical quality, free of inclusions [44].

However, the effective nonlinear coefficient of LBO, which is $\boldsymbol{d}_{\text{eff}}$ = 0.85pm/V, limits its SH conversion efficiency. The second drawback of this crystal is that it is hydrophobic [43]. Main physical and optical properties of LBO crystal are listed in Tables 3.1-3.3.

Table 3.1: Chemical and structural properties of LBO [44].

PROPERTY	**VALUE**
Chemical formula	LiB_3O_5
Crystal Structure	Orthorhombic, Space group Pna21, Point group mm2
Lattice Parameter [Å]	a=8.4473, b=7.3788, c=5.1395, Z=2
Melting Point [℃]	834
Mohs Hardness	6
Density [g/cm3]	2.47
Thermal Conductivity [W/m/K]	3.5
Thermal Expansion Coefficient [/K]	$a_x=10.8x10^{-5}$, $a_y= -8.8x10^{-5}$, $a_z=3.4x10^{-5}$

Table 3.2: Sellmeier equations of LBO [44].

$n_i^2(\lambda) = A + B/(\lambda^2-C))- D\lambda^2+E /\lambda^4$					
	A	B	C	D	E
n_1	2.45414	0.011249	0.01135	0.01459	6.60x10-5
n_2	2.53907	0.012711	0.01252	0.01854	2.0x10-4
n_3	2.58618	0.013099	0.01189	0.01797	2.26x10-4

Table 3.3: Optical and nonlinear optical properties of LBO [44].

PROPERTY	VALUE
Transparency Range [nm]	160-2600
SHG Phase Matchable Range [nm]	551 ~ 2600 (Type I) 790-2150 (Type II)
Thermo-optic Coefficient [°C, l in μm]	$dn_x/dT=-9.3X10^{-6}$ $dn_y/dT=-13.6X10^{-6}$ $dn_z/dT=(-6.3-2.1l)X10^{-6}$
Absorption Coefficient [%/cm]	<0.1 at 1064nm <0.3 at 532nm
Angle Acceptance [mrad-cm]	6.54 (φ, Type I,1064 SHG) 15.27 (θ, Type II,1064 SHG)
Temperature Acceptance [C-cm]	4.7° (Type I, 1064 SHG) 7.5° (Type II,1064 SHG)
Spectral Acceptance [nm-cm]	1.0 (Type I, 1064 SHG) 1.3 (Type II,1064 SHG)
Walk-off Angle	0.60° (Type I 1064 SHG) 0.12° (Type II 1064 SHG)
NLO Coefficient	$d_{eff}(I)=d_{32}\cos\varphi$ (Type I in XY plane) $d_{eff}(I)=d_{31}\cos^2\theta+d_{32}\sin^2\theta$ (Type I in XZ plane) $d_{eff}(II)=d_{31}\cos\theta$ (Type II in YZ plane) $d_{eff}(II)=d_{31}\cos^2\theta+d_{32}\sin^2\theta$ (Type II in XZ plane)

3.2 Potassium Titanyl Phosphate (KTP) Crystal

KTP is one of the most popular crystals for frequency-doubling of 1064nm Nd:YAG lasers. This crystal is also used for sum frequency mixing (SFM); parametric sources of light (OPO, OPG, OPA, optical parametric oscillator, optical parametric generation, optical parametric amplification, respectively) with wavelengths tunable in the 0.6-4.5 μm range; electrooptic modulators; optical switches; directional couplers. Main features of KTP are:

- Large nonlinear optical coefficient.
- Wide angular bandwidth and small spatial walk-off angle.
- Broad temperature and spectral bandwidths.
- High electro-optic coefficient and low dielectric constant.
- Non hygroscopic;
- Good chemical and mechanical properties [44].

After all, the weakness of this crystal is its relatively low damage threshold. Main physical and optical properties of KTP crystal are listed in Tables 3.4-3.6.

Table 3.4: Optical and nonlinear properties of KTP [44].

PROPERTY	VALUE
Transparency Range , [nm]	350 - 4500
Refractive Indices, [nm]	at 1064 $n_x = 1.7377$, $n_y = 1.7453$, $n_z = 1.8297$
	at 532 $n_x = 1.7780$, $n_y = 1.7886$, $n_z = 1.8887$
Thermo-Optic Coefficients [/^oC]	$dn_x/dT = 1.1 \times 10^{-5}$
	$dn_y/dT = 1.3 \times 10^{-5}$
	$dn_z/dT = 1.6 \times 10^{-5}$
Phase-Matchable Output Range [nm]:	492- 1700
Linear Absorption Coefficients, [cm^{-1}]	$\alpha<0.001$ (λ =1064 nm or 532 nm)
NLO Coefficients [pm/V]:	d31=2.54, d32=4.35, d33=16.9, d24=3.64, d15=1.91 at 1064 nm;

Table 3.5: Structural and physical properties of KTP [44].

PROPERTY	VALUE
Chemical formula	$KTiOPO_4$
Crystal Structure	Orthorhombic, point group mm^2
Cell Parameters, [Å]	a = 6.404,b = 10.616, c = 12.814, Z = 8
Melting Point	1172^oC Incongruent
Curie point	936^oC
Mohs Hardness	≈5.0
Density, [g/cm^3]	3.01
Hygroscopic Susceptibility	No

Relative Dielectric Constant, [ε_{eff}]	13
Specific heat [cal/g·^{o}C]	0.1643
Electrical conductivity, [s/cm]	3.5 x 10^{-8} (c-axis,22^{o}C,1KHz)
Thermal Conductivity, [W/m/K]	13

Table 3.6: Sellmeier equations of KTP [44].

$n_i^2(\lambda) = A + B/(\lambda^2-C))- D\lambda^2$				
	A	B	C	D
n_1	3.0065	0.039	0.0425	0.0133
n_2	3.0333	0.0415	0.0455	0.0141
n_3	3.3134	0.0569	0.0566	0.0168

Since coefficient of the effective nonlinearity $\boldsymbol{d_{eff}}$ is too small for Type I phase-matching, this type of phase-matching is not used in practice.

3.3 Monoclinic Bismuth Triborate (BiBO) Crystal

Monoclinic bismuth triborate (BiB_3O_6) is a relatively new crystal material. First studies of BiBO were done by Hellwig and co-workers in 1998 [15]. Its main features are:

- As opposed to LBO crystal, BiBO is non-hygroscopic.
- The transparency of BiBO ranges from 300 nm to 2500 nm.
- Large effective nonlinear coefficient is 3.2 pm/V.
- The spectral acceptance is moderate and ranges between LBO and KTP.

The main weakness of BiBO is its particularly large walk-off angle 28mrad*cm at 1064 nm, and the angular acceptance for BiBO is 2.1 mrad*cm which is much smaller than for KTP and BBO crystals [21].

Table 3.7: Structural and physical properties of BiBO [36, 45, 21].

PROPERTY	VALUE
Chemical formula	BiB_3O_6
Lattice Parameter [Å]	a=7:116 , b=4:993 , and c=6:508
Melting Point (congruent) [℃]	726
Specific Heat [J/g-K]	0.5 at 330 K
Hardness [Mohs]	5 – 5.5
Density [g/cm3]	5.033

Table 3.8: Optical and nonlinear properties of BiBO [36, 45, 21].

PROPERTY	VALUE
d_{eff} [pm/V]	3.2
Temperature Acceptance ΔT l [^{0}Ccm]	2.17
Angle Acceptance ΔΘ l [◦cm]	0.07
Walk-off Angle Δφ l [mrad*cm]	28 at 1050nm
Spectral Acceptance Δλ l [nm*cm]	1.12
losses(λω)[%/cm]	0.09
PM-angle [^{o}]	$\theta = 169$ $\varphi = 90$
ransparency Range [nm]	286-2500
Refractive Indices	
at 1079.5 nm	$n_1 = 1.9166$, $n_2 = 1.7569$, $n_3 = 1.7835$
at 539.75 nm	$n_1 = 1.9260$, $n_2 = 1.7874$, $n_3 = 1.8190$
Optical homogeneity [/cm]	$\sim 10^{-6}$
NLO coefficients (pm/V)	$d_{11} = 2.53$, $d_{12} = d_{14} = 2.3$, $d_{13} = -1.3$,
	$d_{25} = d_{36} = 2.4$, $d_{26} = 2.8$, $d_{35} = -0.9$

Table 3.9: Sellmeier equations of BiBO [45].

$n_i^2(\lambda) = A + B/(\lambda^2-C))- D\lambda^2$				
	A	B	C	D
n_1	3.6545	0.0511	0.0371	0.0226
n_2	3.074	0.0323	0.0316	0.0134
n_3	3.1685	0.0373	0.0346	0.0175

3.4 Periodically Poled Lithium Niobate (PPLN)

Periodically poled lithium niobate (PPLN) is a domain-engineered lithium niobate crystal. In other words this is a bulk $LiNbO_3$ crystal which contains ferroelectric domains that are parallel to the c-direction and have alternating signs from the +*c* to the -*c* direction. Domain period is typically between 5 and 35 μm. The shorter periods of this range are used for second harmonic generation, while the longer ones are used for optical parametric oscillation. Fine-tuning of QPM conditions can be achieved by controlled heating of the crystal through a slight variation of the refractive index dispersion with temperature. For manufacturing of PPLN an electric-field poling technique is commonly used [46]. This method is based on electric-field domain reversal in which a high electric field is applied using lithographically defined electrodes to produce permanent patterns in the bulk $LiNbO_3$ crystal. This technique was first demonstrated by Yamada *et al.* of Sony Corporation in 1992 [47]. Due to the nature of QPM the crystal's axis can be chosen without limitation. For lithium niobate this is done to access d_{33}=27pm/V coefficient. As a result

$$\boldsymbol{d_{eff} = \frac{2}{\pi} d_{33} \approx 17\text{pm/V}} \quad (3.1)$$

For increasing the threshold of photorefractive damage at room temperature and minimizing green-induced infrared absorption, MgO-doping at a concentration of about 5% is added to a congruent lithium niobate (MgO:PPLN).

Table 3.10: Sellmeier equations of PPLN [48].

$n_e^2 = A1 + \text{B1} * f + \frac{A2+B2*f}{\lambda^2-(A3-B3*f)^2} + \frac{100+B4*f}{\lambda^2-A5^2} - A6\lambda^2$						
	A1	A2	A3	A4	A5	A6
n_e	5.35583	0.100473	0.20692	100	11.3493	$1.5334*10^{-2}$
	B1	B2	B3	B4		
	$4.629*10^{-7}$	$3.862*10^{-8}$	$-8.9*10^{-09}$	$2.657*10^{-5}$		

where

$$\boldsymbol{f = (T - T_0)(T + T_0 + 2 * 273.16)} \quad (3.2)$$

The temperature parameter ***f*** is the square of the absolute temperature in degrees Kelvin, with an added offset to make it vanish at the reference temperature T_0 - 24.5.

Table 3.11: Basic optical and nonlinear properties of lithium niobate [45, 49].

Property	Value
Electro-Optical Coefficients, pm/V	r_{33}=30.8, r_{31}=8.6
	r22=3.4, r51=28
Optical Damage Threshold, MW/cm^2	10 – 100
Absorption coefficient, [%/cm]	~0.1 q (1064 nm)
NLO coefficients, [pm/V]	d_{33} = 34.4
	d_{31} = d_{15} = 5.95
	d22 = 3.07
d_{eff} , [pm/V]	17.6 for quasi-phase-matched structures.
Electro-Optic Coefficients ,[pm/V]	g^T_{33} = 32 pm/V, g^S_{33} = 31
	g^T_{31} =10 pm/V, g^S_{31}=8.6
	gT22 = 6.8 pm/V, gS22= 3.4
Linear Absorption coefficient, [%/cm]	0.003-0.01
Damage threshold for 532.1nm [W/m^2]	3.4*10^{-12}
Damage threshold for 1064.2nm [W/m^2]	6.1*10^{-12}

Table 3.12: Basic physical properties of lithium niobate [45, 49].

PROPERTY	VALUE
Chemical formula	MgO:LiNbO3
Crystallographic system	Trigonal, space group R3c
Lattice Constants, Å	a=5.14815 c= 5.1709
Molecular Weight	147.9
Point group	3m
Density, g/cm3	4.644
Transmission Range, μm	0.42 – 5.2
Dielectric Constant	29
Melting Temperature, °C	1255±5
Curie point, °C	1140±5
Thermal Conductivity, W/(m K) at 300 K	5.6
Thermal Expansion, K-1 at 300 K	15×10-6
αa (perpendicular)	4.1×10-6
αc (parallel)	
Specific Heat, cal/(g K)	0.15
Hardness (Mohs)	~5
Bandgap, eV	4
Solubility in water	None

4. Frequency Doubling with LBO, BiBO, KTP, and PPLN Crystals

4.1 Experimental Setup

The passively Q-switched Nd:YAG laser (Teem Photonics) consists of a slice of gain material (Nd^{3+}:YAG) covered by a thin layer of saturable absorber (Cr^{4+}:YAG). This laser operated at 1064 nm and delivered 560 ps long pulses with 10 μJ energy at a repetition rate of 6.9 kHz. This corresponds to a 69 mW of average output power. The temporal pulse profile is shown in Figure 4.1 and was measured with a 6 GHz oscilloscope and a fast photodetector. The spectral characteristics of the laser output are presented in Figure 4.2. As can be seen, the laser operated on two longitudinal modes with the most intense one centered at ~1064.03 nm. The output radiation was linearly polarized and had a TEM_{00} mode structure as illustrated in Figure 4.3.

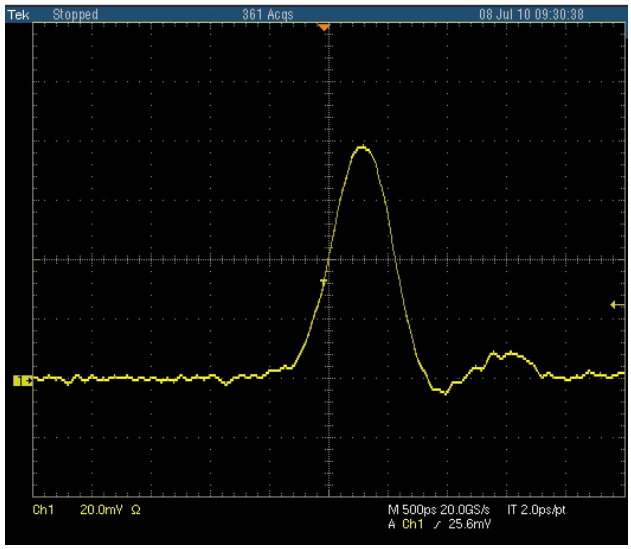

Figure 4.1 Temporal profile of the pump pulse.

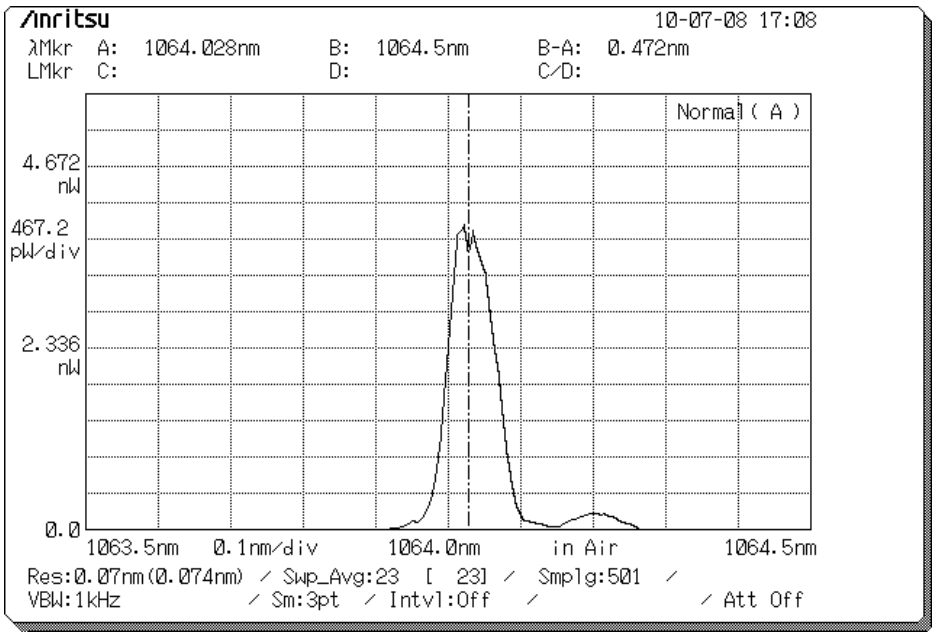

Figure 4.2: Output spectrum of the passively Q-switched Nd:YAG laser (Teem Photonics).

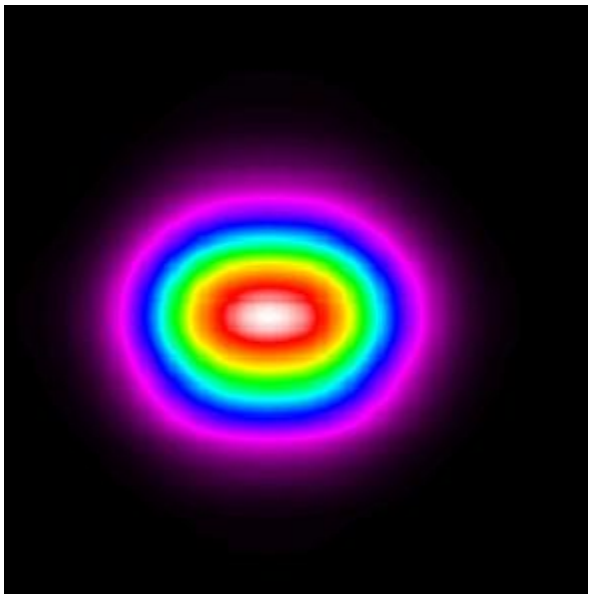

Figure 4.3: Spatial intensity profile of a laser beam from the passively Q-switched Nd:YAG laser (Teem Photonics).

The schematic design of the SHG experiments is presented in Figure 4.4. Initially, the laser beam was directed through an optical attenuator formed by a half wave plate and a polarizing beam splitter. To optimize SHG process, several different focusing conditions were used during the experiments. The radiation was focused by a set of five spherical lenses with focal lengths ranging between 30 mm and 150 mm. This focusing arrangement provided beam waist radii in the 14-109 μm range. Therefore the resultant setup allowed for changing the spot size inside the crystal as well as the input pump power. The maximum output power at fundamental wavelength that was available for the experiments was reduced to 66.3 mW owing to the losses associated with the introduced optical components.

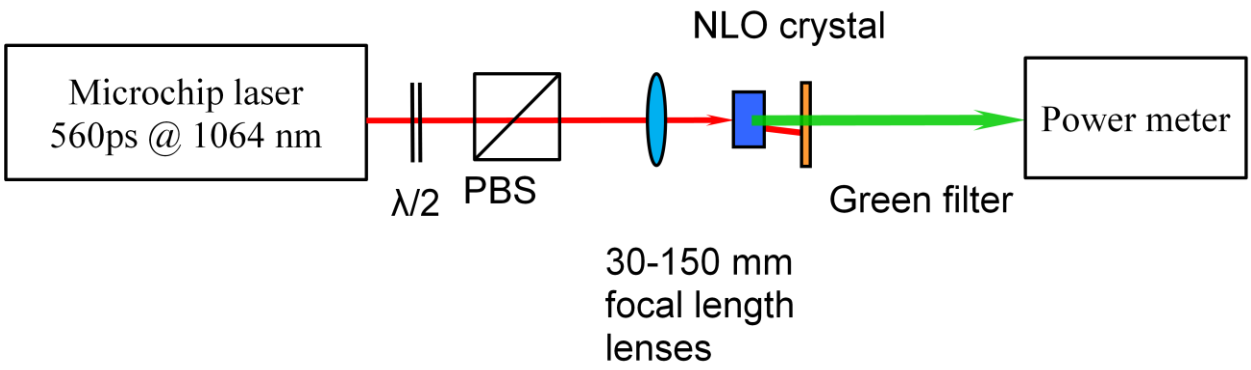

Figure 4.4: Schematic setup for frequency doubling experiments with LBO, KTP, and BiBO .

Crystals were mounted in a vertical rotary mount for precise alignment with respect to incoming polarization of the fundamental radiation. The generated SH was separated from the fundamental wavelength by a dielectric filter. The filter had more than 99.9% reflectivity at 1064 nm and 94.5% transmission at the 532 nm. The 5.5% loss of green radiation at the dielectric filter was

taken into account when estimating the total amount of generated second harmonic. A photograph of the experiments is shown below in Figure 4.5.

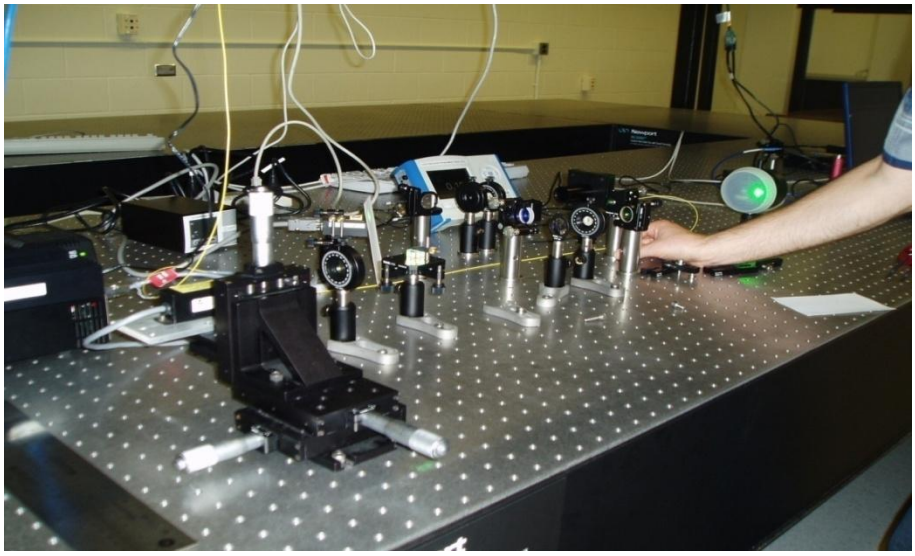

Figure 4.5: Experiment for frequency doubling of Nd:YAG laser with LBO, KTP and BiBO crystals.

The fundamental and produced green radiation was measured by a calibrated thermopile power meter. The spatial beam profiles of the fundamental and SH beams were characterized by a CCD camera.

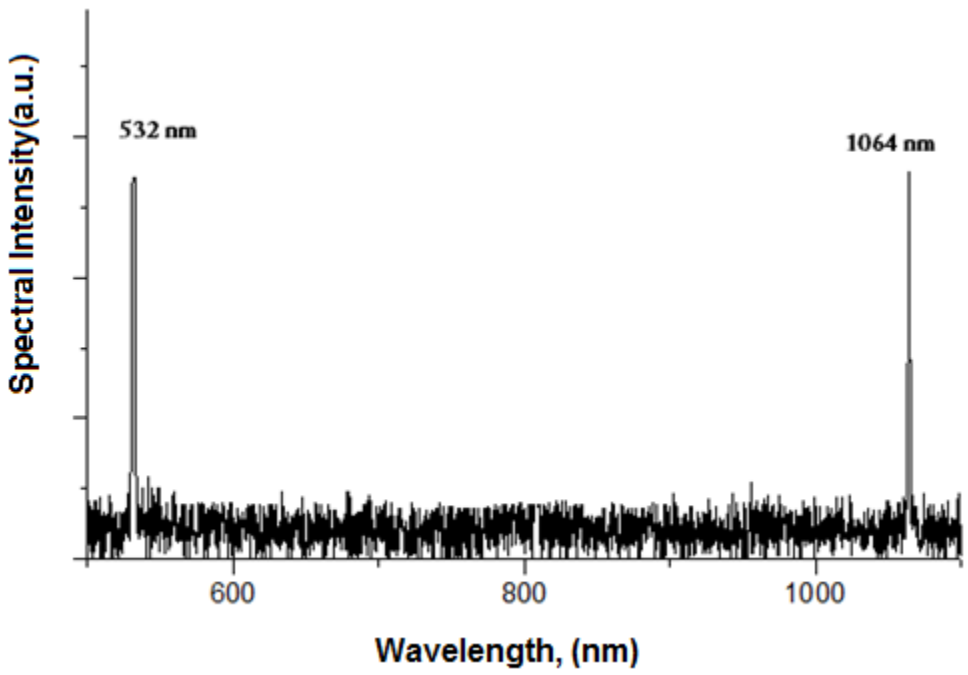

Figure 4.6: Typical spectra of the incident and generated second harmonic radiation.

The laser spectra were measured with a calibrated spectrometer. The intensity of the signals was reduced by the neutral density filters to comply with the sensitivity of the Si detector over the desired wavelength range.

All crystals that were used in the experiments were 5 mm long and had both of their faces antireflection coated for fundamental and SH radiation to reduce reflection losses. All focusing lenses were plano-convex and also were antireflection coated for fundamental and SH radiation.

4.2 KTP Experiments

The KTP crystal was cut at angles of $\theta = 90^0$ and $\varphi = 26^{\mathbf{o}}$ for type II phase matched SHG at 1064nm. Crystal had the dimensions of 5x3x3mm (i.e. 5 mm long). At first the optimum focusing conditions for efficient SHG were investigated. This was done by using several focusing lenses with different focal lengths and recording the maximum average output power of the produced second harmonic for each of them. For each measurement the maximum input pump power was used. The results are shown in Figure 4.7.

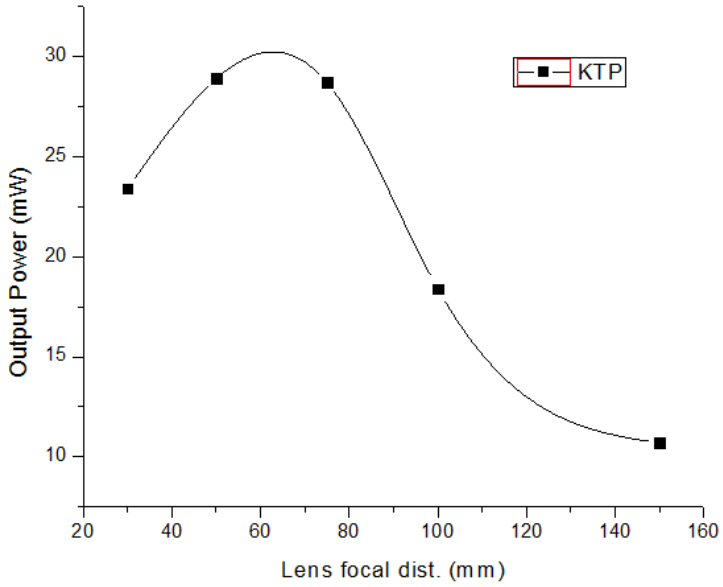

Figure 4.7: Second harmonic output power at 532 nm versus lens focal length.

As can be expected, the output power of the SH strongly depends on the focal length of a lens. The highest output power of 28.9 mW at 532 nm was recorded using a 50 mm focal length lens.

This corresponds to a beam spot size diameter of 50 μm inside the crystal. Focal length range where maximum could be achieved lies between 50 and 75 mm.

The average output power of the generated second harmonic as a function of the incident pump power under optimum focusing condition is presented in Figure 4.8. In this case a 50 mm focal length lens was used. The input power was adjusted by rotating a half waveplate in combination with a polarizing beam splitter. First, at the lowest pump power level, the position of the crystal was optimized with respect to the pump beam waist in order to get the highest SH output power. Next, the fundamental power was gradually increased while recording the SH power. The position of the crystal was not changed during this measurement.

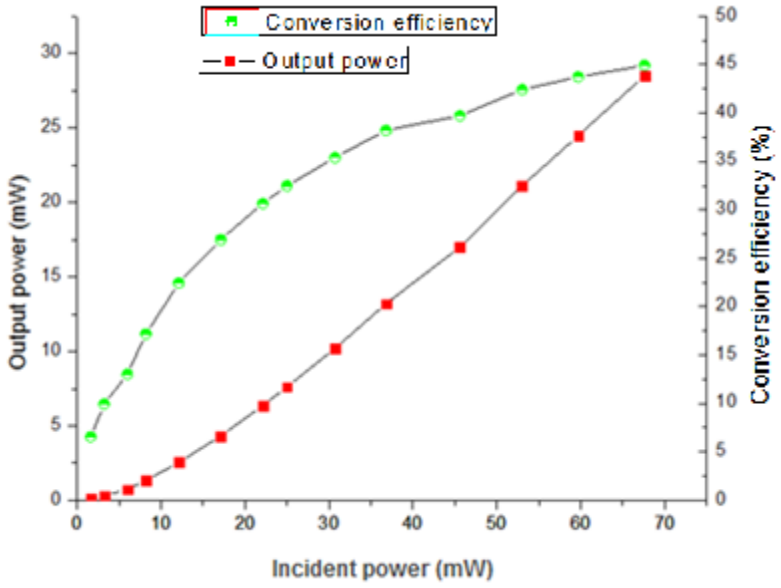

Figure 4.8: Second harmonic output power at 532 nm and conversion efficiency versus incident power with 50 mm focal length focusing lens.

In the experiments it was observed the expected quadratic dependence of the SH power on the input pump power. Efficiency of the process is also steadily increasing with the input power. In this case the maximum conversion efficiency (~45%) is limited by the current level of input power and the depletion of the fundamental wave.

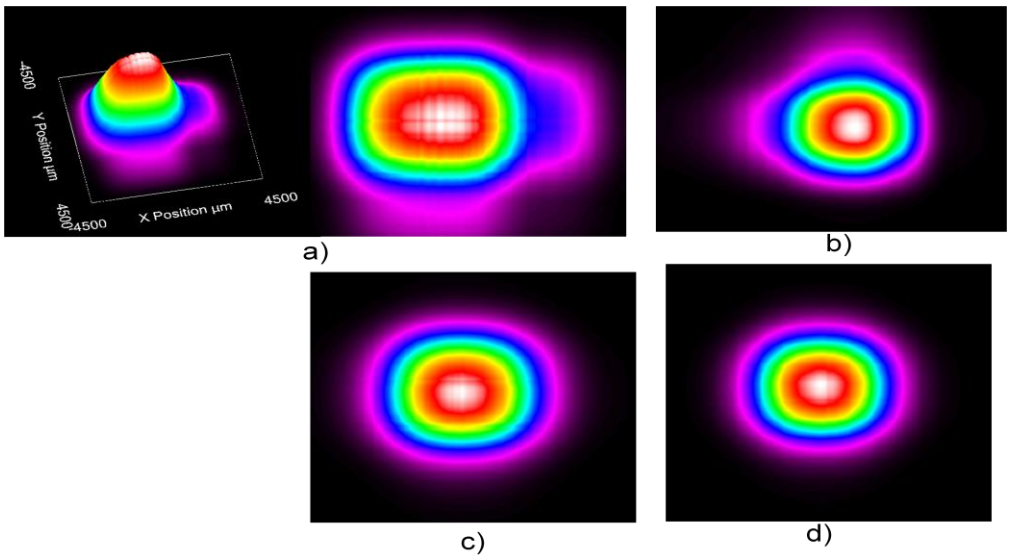

Figure 4.9: Spatial beam profiles of SH produced in KTP for different focusing lenses. a) focal distance 30 mm, 3D&2D; b) focal distance 50mm, 2D; c) focal distance 75 mm, 2D; d) focal distance 100 mm, 2D.

Spatial intensity profiles of the generated second harmonic were studied using a CCD camera. Four intensity profiles are displayed in Figure 4.9. In the first case (a) a lens with 30 mm focal length was used to produce SH with tight focusing conditions. As can be seen the central part of the generated beam of second harmonic still has a TEM_{00} mode structure, but it is no longer circular. It is elongated along the horizontal axis with ellipticity of approximately 1:1.5. This can

be explained by the effect of spatial walk-off. On the contrary, when loose focusing conditions were created using a lens with 75 mm (c) or 100 mm (d) focal lengths the beam shape appeared more circular and symmetrical with a nice TEM_{00} mode structure. In this case loose focusing produces larger beam size inside the crystal which makes contribution of spatial walk-off less noticeable. For all subsequent experiments we used the same procedures that were described above.

4.3 LBO Experiments

The LBO crystal had the dimensions 5x3x3mm (5 mm long) and was cut for type I phase matching at angles of $\theta = 90^0$ and $\varphi = 12.4^0$. A maximum output power of 10.2 mW at 532 nm was achieved using a lens with the focal length of 50 mm (Figure 4.10). This corresponds to a conversion efficiency of 16% with respect to the maximum available infrared power.

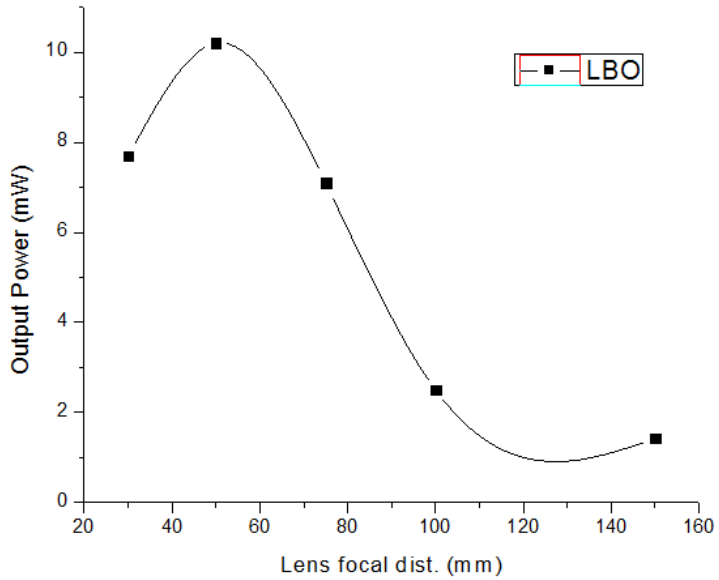

Figure 4.10: Second harmonic output power at 532 nm versus lens focal length.

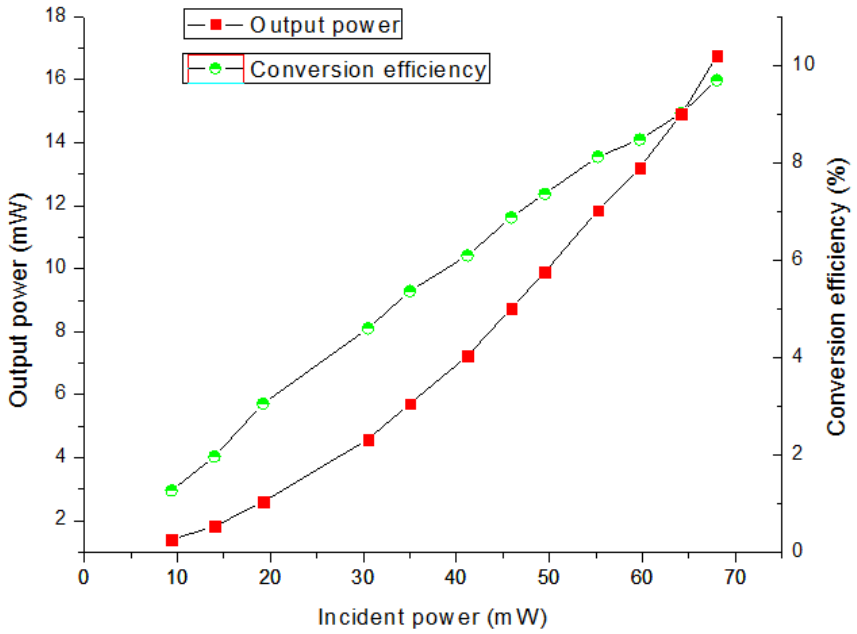

Figure 4.11: Second harmonic output power at 532 nm and conversion efficiency versus incident pump power with 50 mm focal length focusing lens.

Figure 4.11 shows that the SHG output power increased nonlinearly (quadratically) with the pump power. Since low nonlinearity of LBO results in low conversion efficiency, its saturation was not observed.

Spatial beam profiles of the generated SH are presented in Figure 4.12. They have similar to KTP dependence on focusing. In case where the lens with 30 mm focal length was used we still had the central part of the generated beam as a TEM_{00} mode structure, but it is no longer circular (Figure 4.12 a) . It is elongated along the horizontal axis with ellipticity of approximately 1:2.

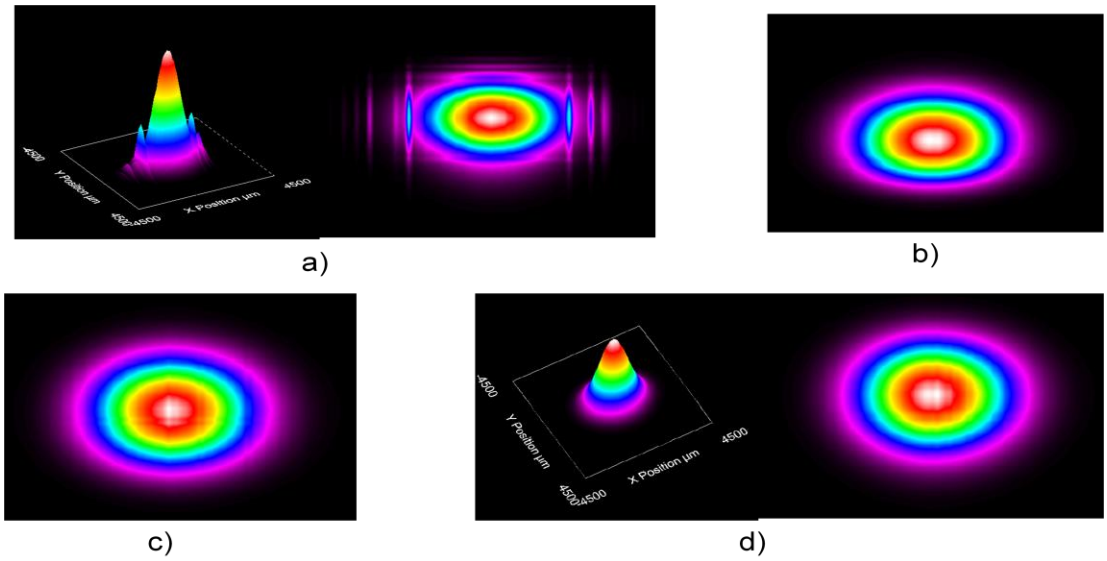

Figure 4.12: Spatial beam profiles of SH at 532 nm produced in LBO crystal using different focusing lenses. a) focal distance 30 mm, 3D&2D; b) focal distance 50 mm, 2D; c) focal distance 75 mm, 2D; d) focal distance 100 mm, 2D&3D.

At the same time two side lobes appeared in the horizontal plane resembling a $sinc^2$-like function. These optical beam distortions caused by the strong focusing conditions can be explained by the spatial beam walk-off and limited angular acceptance of the crystal, respectively.

4.4 BiBO Experiments

The BiBO crystal was 5 mm long (with 3x3 mm^2 cross section) and antireflection coated at the fundamental and second harmonic (SH) wavelengths. The crystal was cut for type-I critically phase-matched interaction with the effective nonlinearity of 3.2 pm/V for $\varphi = 90\circ$, $\theta = 169^0$.

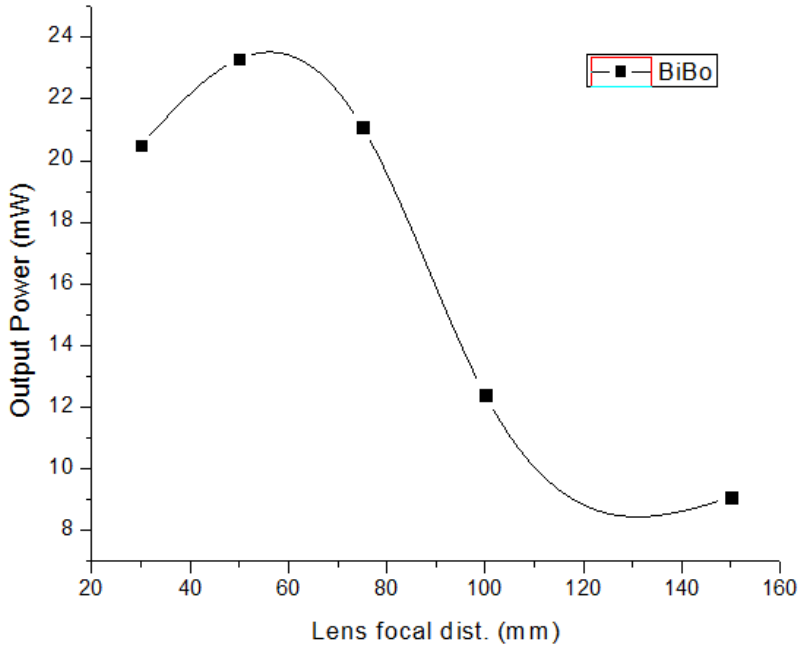

Figure 4.13: Dependence of the second harmonic output power on focusing conditions.

Figure 4.13 shows how the output power of SH depended on the lens focal length. Similar to the previous cases the maximum output of SH was achieved with 50 mm focusing lens. This lens was used for the following experiment.

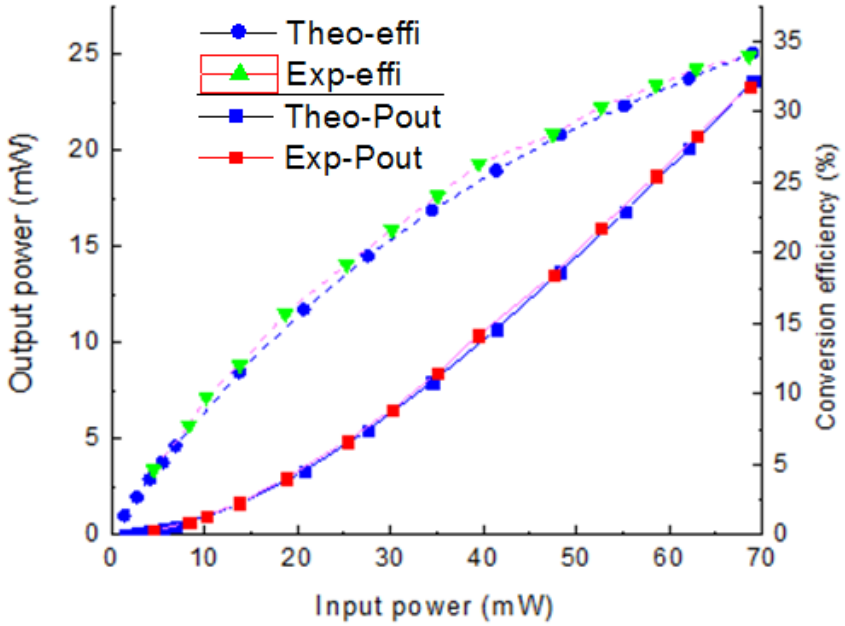

Figure 4.14: Second harmonic output power (red squares - experimental data and blue squares – theory) at 532 nm and conversion efficiency (green triangles – experimental data and blue circles - theory) versus incident power using a focusing lens with 50 mm focal length.

On the Figure 4.14 we can observe the expected quadratic dependence of the SHG power on the input pump power. Efficiency of the process was also steadily increasing with the input power and started to show signs of saturation at high power. In this case the maximum conversion efficiency was also limited by the current level of input power and depletion of the pump. The highest output power recorded was 23.3 mW at 532 nm. This corresponds to a beam spot size diameter of 50 μm inside the crystal.

Experimental data for BiBO crystal were compared against theoretical calculations performed using a freely available SNLO software package from Sandia National Laboratories,

Albuquerque, USA. Experimental and theoretical data are in very good agreement as displayed in Figure 4.14.

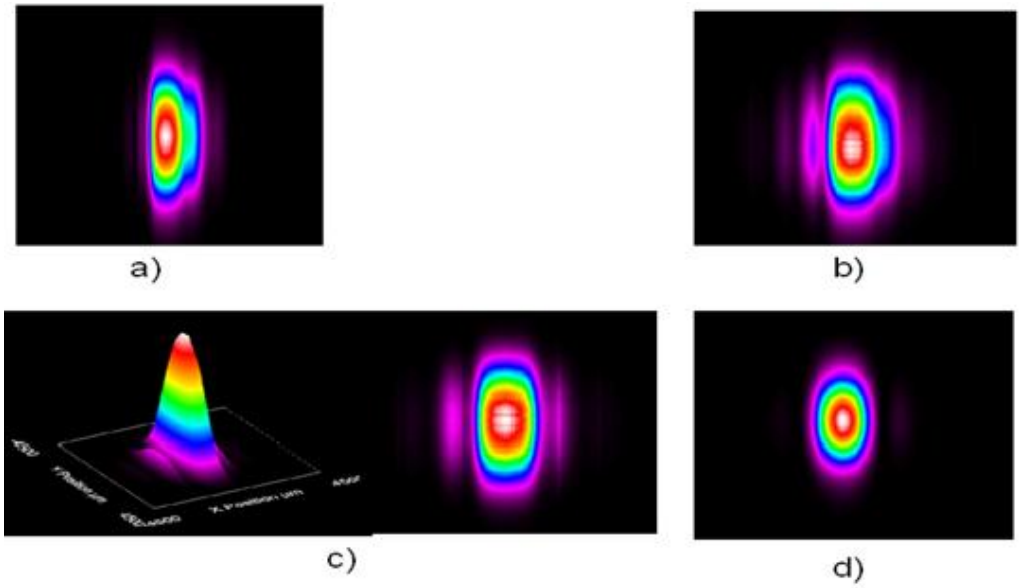

Figure 4.15: Variation of spatial beam profiles of SH with focusing conditions in BiBO crystal. a) focal distance 30 mm, 2D; b) focal distance 50 mm, 2D; c) focal distance 75 mm, 2D&3D; d) focal distance 100 mm, 2D.

Four spatial beam profiles for the BiBO crystal are displayed in Figure 4.15. On the picture (d) a lens with 150 mm focal length was used to produce SH with loose focusing conditions. The beam shape appeared elongated with a nice TEM_{00} mode structure. When more tight focusing conditions were created using a lens with 75 mm focal length (c), the central part of the generated beam of second harmonic still had a TEM_{00} mode structure but it was no longer circular. It was elongated along the vertical axis with ellipticity of approximately 1:2. In case of b) and a) When we created even tighter focusing conditions with 50 mm (b) and 30 mm (a)

lenses, we saw the further degradation of the beam. The optical beam distortions caused by the strong focusing conditions are similar to those observed in LBO crystal and also can be explained by the spatial beam walk-off and limited angular acceptance of the crystal, respectively.

5. Frequency Doubling with PPLN Crystal

The MgO-doped PPLN crystal from C2C Link Corporation was 5 mm long, 2 mm wide and 0.5 mm thick crystal with a period grating of 7 μm. The two end faces of the crystal were antireflection coated for both 1064 nm and 532 nm wavelengths. The crystal was mounted on a temperature controller with a temperature stability of ±0.1 °C. The optimal phase matching temperature was found to be 32.8 °C, which is a little higher than the nominal 29.9 °C perhaps due to the imperfect contact between the crystal and the temperature controller. A schematic of the experimental setup is illustrated in Figure 5.1.

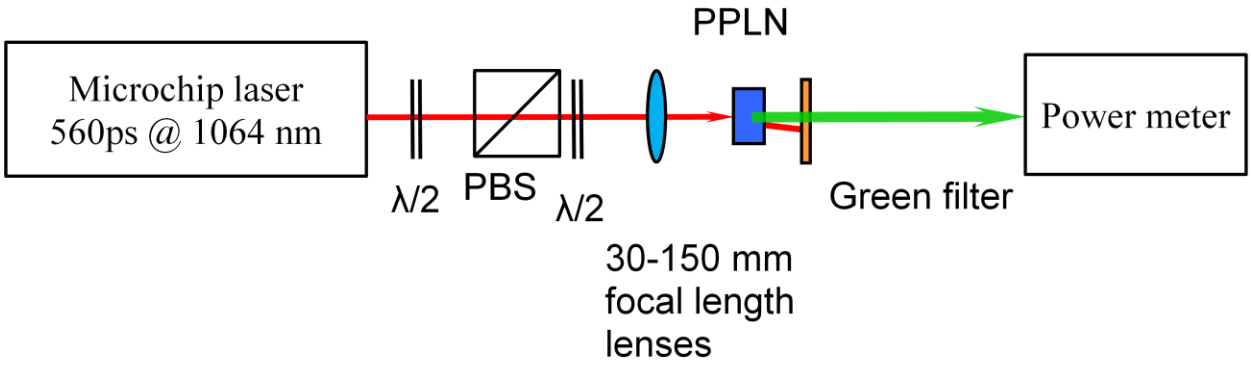

Figure 5.1: Schematic setup for frequency doubling experiments with PPLN.

As before, the first half-wave plate and a polarizing beam splitter were used for controlling the incident power into the nonlinear crystal. The second half-wave plate altered polarization of the pump beam to extraordinary one (vertical in our case) to match the QPM interaction in the MgO:PPLN crystal. The pulse temporal trace was detected by InGaAs photodiode (100 ps

raising time and 100 ps falling time), and recorded by a digital oscilloscope (Tektronix TDS6604, 6 GHz bandwidth). The spatial beam profile was recorded by a CCD beam profiler.

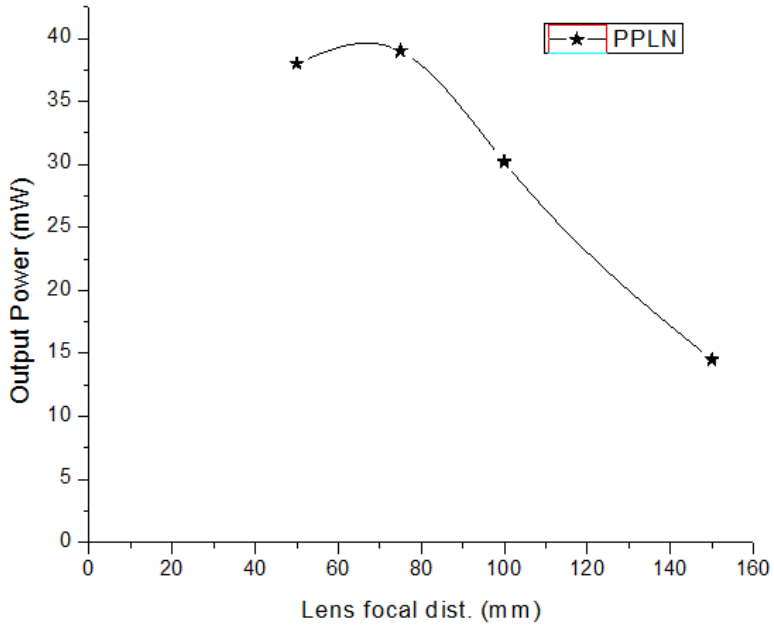

Figure 5.2: Dependence of SH output power on lens focal distance.

Without any focusing lenses (laser output had a waist of 300 μm in diameter), the MgO:PPLN crystal delivered 36.4 mW of green light with 66.5 mW of incident pump power. This corresponds to an optical-to-optical conversion efficiency of 55%. To optimize the SHG, the same plano-convex antireflection coated lenses with focal lengths ranging from 50 mm to 150 mm were used. The obtained SH output power dependence is shown in Figure 5.2.

The lenses focused the pump beam into the crystal with waist radii between 24.8 μm and 109.2 μm. Using the lens with 75 mm focal length, the maximum output power of 38.5 mW was

obtained, corresponding to 60% conversion efficiency. Therefore, the lens with 75 mm focal length was selected for the following measurement.

The second harmonic output power as a function of the incident power was measured as illustrated in Figure 5.3. By rotating the first half-wave plate, the incident power can be tuned up to 64 mW continuously. The output power increased quadratically with the increase of incident power as expected. The maximum output average power of 38.5 mW with pulse energy of 5.6 µJ is obtained. This corresponds to an optical-to-optical conversion efficiency of 60% (Figure 5.3).

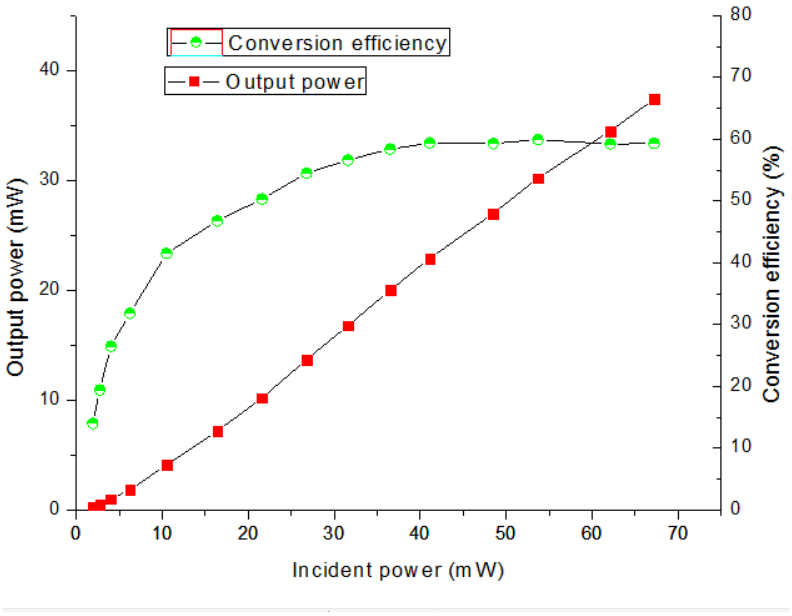

Figure 5.3: Second harmonic output power at 532 nm and conversion efficiency versus incident power under 75 mm focal length lens focusing condition.

The conversion efficiency also increased gradually but saturated after the incident power reaches ~30 mW, corresponding to a pulse energy of 4.4 µJ. At this low power level thermal effects that can arise from the absorption of laser radiation and alter phasematching conditions are

negligible. Therefore the depletion of the pump power was the main reason for the saturation of the efficiency. Theoretical modeling of SHG in MgO:PPLN crystal was not possible because SNLO software does not support QPM interactions. The general trend observed in the experiments, however, is very similar to the cases of KTP and BiBO crystals and qualitatively supports our statement.

Figure 5.4 shows the spatial beam profiles of second harmonic radiation. The fundamental beam has TEM_{00} mode structure, therefore appeared as a circular and symmetric shape. At the maximum output power under tight focusing condition (a,b), the shape of the SH beam was almost circular, even though it was a little distorted. The beam profile of the second harmonic radiation, however, was much better than that from the BiBO crystal that was used previously. This was caused by the absence of the spatial walk-off effect in periodically poled crystal (i.e. non-critical phasematching condition was used). Please note that distortion of the beam in case (c) is caused by misalignment of the crystal which was only 0.5 mm thick.

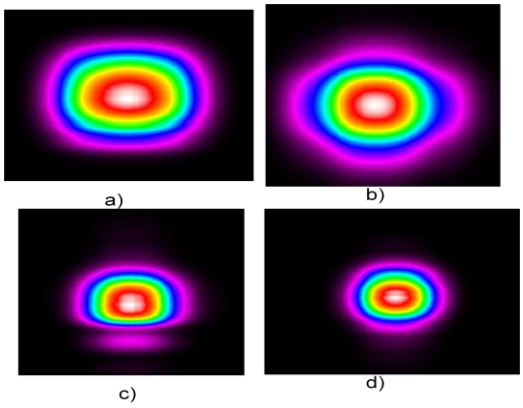

Figure 5.4: Spatial beam profiles of SH at 532 nm produced in MgO:PPLN crystal using different focusing lenses. a) focal distance 50 mm; b) focal distance 75 mm; c) focal distance 100 mm; d) focal distance 150 mm.

The temperature acceptance of the MgO:PPLN crystal was also examined and the results are presented in Figure 5.5.

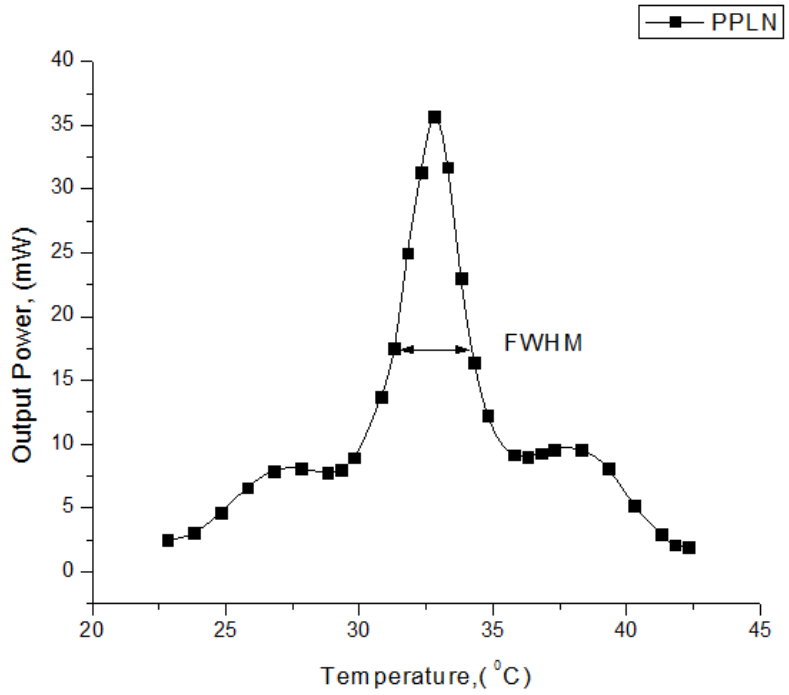

Figure 5.5: Second harmonic output power at 532 nm as a function of temperature of the MgO:PPLN crystal.

The temperature tuning curve resembles a sinc^2 function shape as was discussed earlier in Section 2.7.3. The FWHM of the curve is around 3 °C. Theoretical temperature acceptance can be calculated by using the modified equation 2.29 [50]:

$$\Delta T = \frac{0.4429\lambda_{\omega}}{L}\left[\frac{\partial n_{2\omega}}{\partial T} - \frac{\partial n_{\omega}}{\partial T} - \alpha(n_{2\omega} - n_{\omega})\right]^{-1} \tag{5.1}$$

where L is the crystal length, λ_ω is the pump wavelength, α is the thermal expansion coefficient of the crystal, and $n_{2\omega}$ and n_ω are the extraordinary refractive indices calculated from the latest Sellmeier equations [51]. At the phasing matching temperature of 32.8 °C the theoretical width of the tuning curve is 5.8 °C, which is almost twice larger than the measured value. One of the possible reasons for this discrepancy may come from the non uniformity of the grating pattern in the crystal. Another reason might be related to the non uniform temperature distribution in the crystal, which can be caused by a loose contact between the crystal and the heating block.

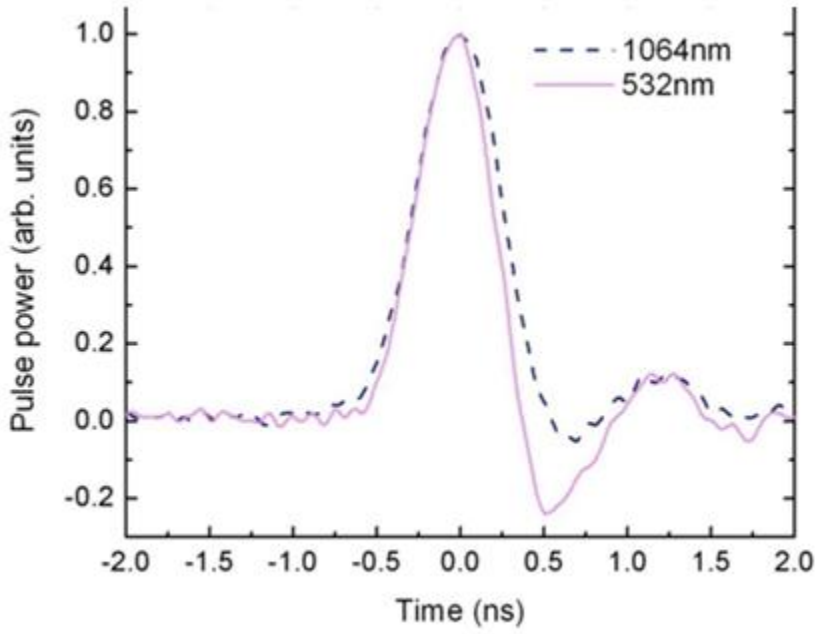

Figure 5.6: Temporal profiles of the pump and SH pulses at the maximum output power of 38 mW at 532 nm.

The temporal profiles of the fundamental and second harmonic pulses are displayed in Figure 5.6. The secondary pulses are caused by electrical “ringing”. The measured pulse duration for the

second harmonic pulses was 510 ps, which is a little shorter than 560 ps for the fundamental pulses. This pulse shortening effect is a common feature in SHG and was also observed with microchip lasers [1,13]. The results of the experiments with MgO:PPLN crystal are being prepared for a journal publication [52].

6. Summary of Results and Discussion

In this section we will review all results obtained for SHG in crystals of LBO, KTP, BiBO, and MgO:PPLN. The main results are summarized in Figures 6.1, 6.2, 6.3, 6.4, and Table 6.1.

In our experiments we found that all crystals exhibited strong dependence of SHG process on the focal length of a focusing lens. This procedure was used to find optimum focusing conditions for SHG process. For example, as shown in Figure 6.1, for KTP, LBO, and BiBO the maximum SH output powers were reached with the 50 mm focal distance lens. For MgO:PPLN the best result was obtained at 75 mm. Since each point in Figure 6.1 corresponds to the highest achieved output power of SH and the same maximum input power was used for all measurements, the maximum conversion efficiency would have the same dependence on the focusing conditions as the second harmonic output power. In this respect crystals of MgO:PPLN and KTP were the most efficient (up to 60%).

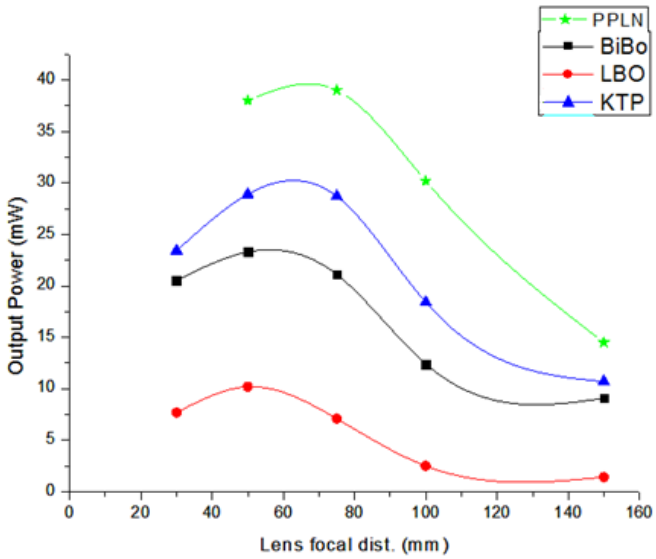

Figure 6.1: Dependence of the second harmonic output power on focusing conditions.

The dependence of the second harmonic output power at 532 nm versus the incident pump power at 1064 nm is displayed in Figure 6.2. In the experiments at low input powers we observed the expected quadratic dependence of the SH power on the input pump power for all crystals. For higher levels of input power the SH output power dependence was more linear. The highest SH output power of 38.5 mW was obtained for MgO:PPLN crystal, which has the largest nonlinearity among the used crystals. Unfortunately, focusing lenses in the range between 50 – 75 mm focal lengths where not available during the experiments to optimize SHG efficiency even further.

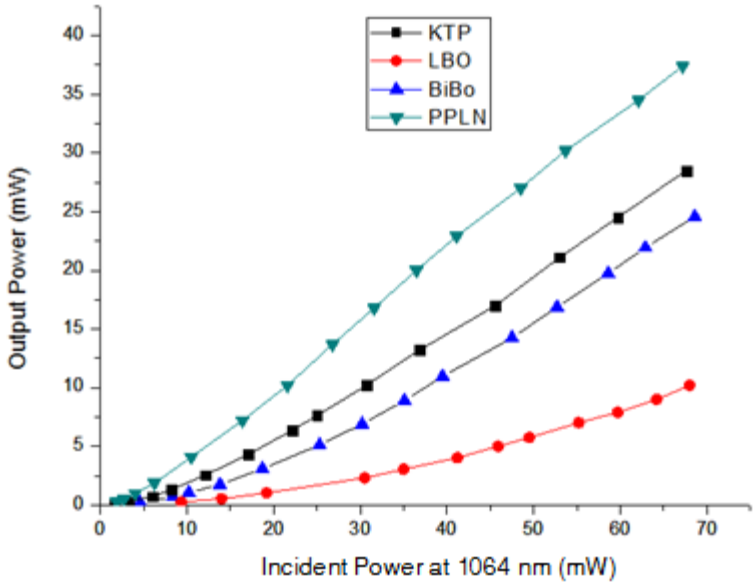

Figure 6.2: Second harmonic output power at 532 nm versus incident power at1064 nm.

Another way to represent data of Figure 6.2 is to look at the SHG efficiency. Such analysis is presented in Figure 6.3. It can be seen that conversion efficiency was linearly increasing with the input power as expected from the Equation 2.25. At higher levels of input power, however,

conversion efficiency starts to show signs of saturation. This is particularly evident for the MgO:PPLN crystal. The cause of saturation can be attributed mainly to the depletion of the fundamental radiation. At the same time the maximum conversion efficiency (up to 60% for MgO:PPLN) was limited by the current level of the available input power. The maximum SHG efficiencies are summarized in Table 6.1.

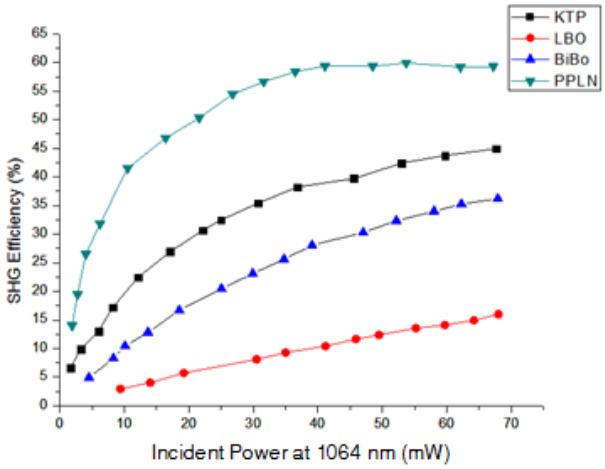

Figure 6.3: Dependence of the second harmonic efficiency versus input power.

Table 6.1: Maximum SH conversion efficiency for NLO crystals.

NLO Crystal	Maximum SHG Efficiency (%)
LBO	16
BiBO	36
KTP	45
MgO:PPLN	60

Spatial intensity profile of the generated second harmonic was studied using a CCD camera. For each of the four crystals two intensity profiles are displayed in Figure 6.4. In the first case (upper row) the lens with 150 mm focal length was used to produce SHG with loose focusing conditions. While the beam shape mainly appears to be circular and symmetrical with a nice TEM_{00} mode structure, the output from the BiBO crystal was significantly reshaped owing to the effect of spatial walk-off.

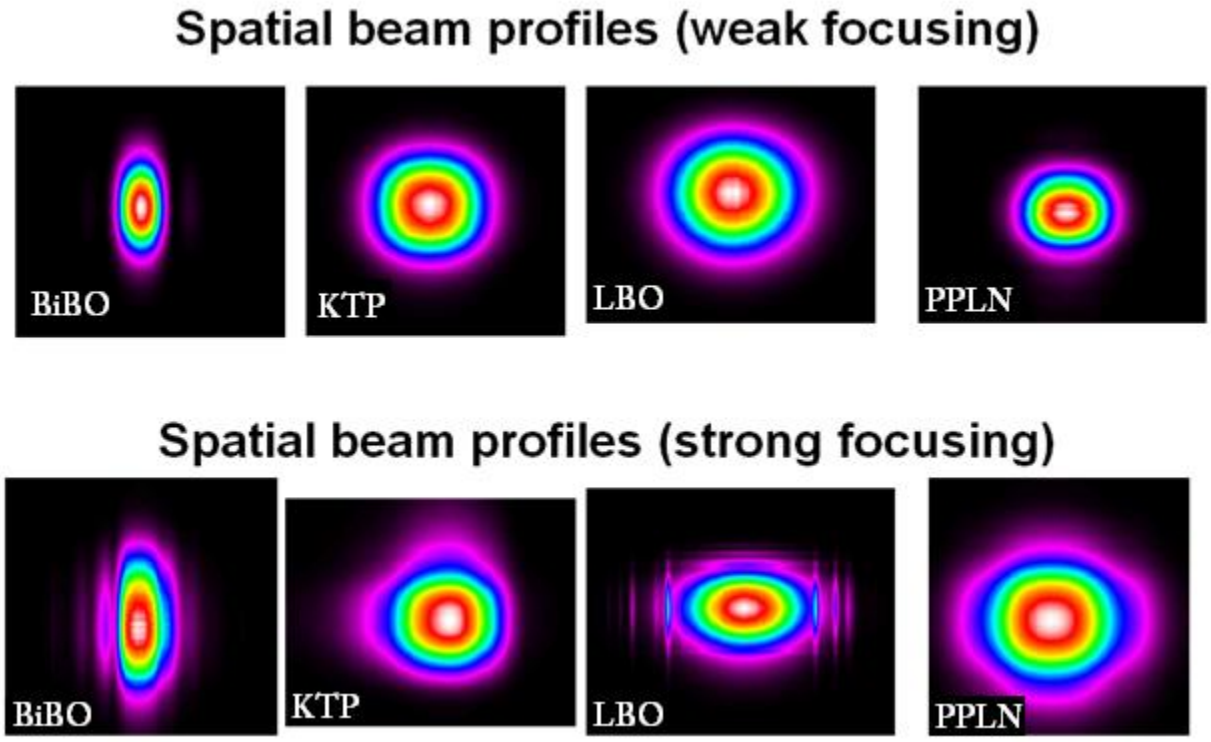

Figure 6.4: Comparison of spatial beam profiles for weak and strong focusing conditions.

For the second case (lower row) strong focusing conditions were created using the lens with 50 mm focal length. In case of BiBO and LBO crystals the central part of the generated beam of second harmonic still had a TEM_{00} mode structure, but several side lobes appeared in the horizontal plane resembling a $sinc^2$-like function. This was a result of limiting action from the

angular acceptance of the crystal. Such behavior was not observed for KTP and MgO:PPLN crystals which are characterized by wide angular acceptances.

Conclusions

In conclusion, a highly efficient frequency doubling of Q-switched microchip laser was demonstrated using crystals of MgO:PPLN, BiBO, KTP, and LBO. This efficient, compact, economic sub-nanosecond green laser source is suitable for many biomedical applications such as spectroscopy, microscopy and biosensors. To get the best performance in second harmonic generation, different focusing conditions were explored. The optical-to-optical conversion efficiency reached 60% which is to the best of our knowledge, is the highest value for pulsed green light generation using the MgO:PPLN crystal. The measured temperature acceptance of the crystal is around 3 °C, which was smaller than the theoretical value. The shape of the output beam was a little distorted but is almost circular and symmetric.

Relatively recently developed BiBO nonlinear crystal was also studied. Such frequency conversion regime for BiBO crystals was investigated for the first time. Generation of green sub-nanosecond pulses with 3.4 μJ energy and efficiency up to 36 % was achieved. While stronger focusing resulted in higher conversion efficiency, the spatial intensity profile of the second harmonic was reshaped owing to a finite angular acceptance and spatial walk-off in the crystal. The SHG performance of the MgO:PPLN and BiBO crystals was compared to that of the more widely used crystals of KTP and LBO.

The combination of high conversion efficiency and good beam quality make MgO:PPLN superior to the birefringent phase matched crystals presented in this study, although this crystal needs precise temperature control. At the same time high energy (~1-500 mJ) SHG process would benefit from BiBO crystal since it has a larger aperture than MgO:PPLN and higher damage threshold than KTP.

References

[1] J. J. Zayhowski and C. Dill III, "Diode-pumped passively Q-switched picosecond microchip lasers," Opt. Lett. **19**, 1427 (1994).

[2] J.L. Li, D. Lin, L.X. Zhong, K. Ueda, A. Shirakawa, M. Musha, and W.B. Chen," Passively Q-switched Nd:YAG ceramic microchip laser with azimuthally polarized output", Laser Phys. Lett. **6**, 711 (2009).

[3] A. Steinmetz, D. Nodop, J. Limpert, R. Hohmuth,W. Richter, and A. Tünnermann," 2 MHz repetition rate, 200 ps pulse duration from a monolithic, passively Q-switched microchip laser", Appl. Phys. B **97**, 317 (2009).

[4] V. E. Kisel', A. S. Yasyukevich, N. V. Kondratyuk, and N. V. Kuleshov, "Diode-pumped passively *Q*-switched high-repetition-rate Yb microchip laser", IEEE J. Quantum Electron. **39**, 1018 (2009).

[5] M. Okuno, H. Kano, P. Leproux, V. Couderc, and H. Hamaguchi, "Ultrabroadband multiplex CARS microspectroscopy and imaging using a subnanosecond supercontinuum light source in the deep near infrared," Opt. Lett. **33**, 923 (2008).

[6] P. Champert, V. Couderc, P. Leproux, S. Février, V. Tombelaine, L. Labonté, P. Roy, C. Froehly, and P. Nérin, "White-light supercontinuum generation in normally dispersive optical fiber using original multi-wavelength pumping system," Opt. Express **12**, 4366 (2004)

[7] B. Rankin, R. Kellner, and S. Hell, "Stimulated-emission-depletion microscopy with a multicolor stimulated-Raman-scattering light source," Opt. Lett. **33**, 2491 (2008)

[8] S. Lévêque-Fort, D. Papadopoulos, S. Forget, F. Balembois, and P. Georges," Fluorescence lifetime imaging with a low-repetition-rate passively mode-locked diode-

pumped Nd:YVO4 oscillator", Opt. Lett. **30**, 168 (2005).

[9] B. Kaehr, N. Ertaş, R. Nielson, R. Allen, R. Hill, M. Plenert, Jason B. Shear, "Direct-write fabrication of functional protein matrixes using a low-cost Q-switched laser", Anal. Chem. **78**, 3198 (2006).

[10] A. Major, V. Barzda, P. A. E. Piunno, S. Musikhin, and U. J. Krull, "An extended cavity diode-pumped femtosecond Yb:KGW laser for applications in optical DNA sensor technology based on fluorescence lifetime measurements," Opt. Express **14**, 5285 (2006).

[11] A. Major, K. Sukhoy, H. Zhao, and I. T. Lima Jr.," Green sub-nanosecond microchip laser based on BiBO crystals", Laser Phys. **21**, 57 (2010)

[12] F. Druon, F. Balembois, P. Georges, and A. Brun," High-repetition-rate 300-ps pulsed ultraviolet source with a passively Q-switched microchip laser and a multipass amplifier", Opt. Lett. **24**, 499 (1999).

[13] J. J. Zayhowski, "Periodically poled lithium niobate optical parametric amplifiers pumped by high-power passively *Q*-switched microchip lasers," Opt. Lett. **22**, 169 (1997).

[14] H. Jing-liang *et al.***,** "Continuous-wave output of 5.5 W at 532 nm by intracavity frequency doubling of an Nd:YVO_4 laser " , Chinese Phys. Lett. **15**, 418 (1998)

[15] H. Hellwig, J. Liebertz, and L. Bohaty, "Exceptional large nonlinear optical coefficients in the monolclinic bismuth borate BiB_3O_6 (BiBO)", Solid State Comm. **109**, 249 (1999)

[16] Y.F. Lü, X.H. Zhang, R. Chen, J. Xia, J.F. Chen, Z.T. Liu, " Diode-pumped Nd:YAG/BiB_3O_6 deep-blue laser at 449.5 nm ",Laser Phys. Lett. **7**, 347 (2010).

[17] Y. Lü, G. Sun, X. Fu, J. Xia, J. Chen, T. Zheng,” Diode-pumped CW frequency-doubled Nd:CNGG-BiBO blue laser at 468 nm ”, Laser Phys. Lett. **7**, 495 (2010).

[18] C. Du, B. Teng, Z. Wang, J. Liu, X. Xu, G. Xu, K. Fu, J. Wang, Y. Liu, Z. Shao,” Actively *Q*-switched intracavity second-harmonic generation of 1.06 μm in BiB_3O_6 crystal”, Opt. Laser Tech. **34**, 343 (2002).

[19] S. Johansson, S. Bjurshagen, C. Canalias, V. Pasiskevicius, F. Laurell, R. Koch, "An all solid-state UV source based on a frequency quadrupled, passively Q-switched 946 nm laser," Opt. Express **15**, 449 (2007).

[20] Z. Wang, B. Teng, K. Fu, X. Xu, R. Song, C. Du, H. Jiang, J. Wang, Y. Liu, Z. Shao, “Efficient second armonic generation of pulsed laser radiation in BiB3O6 (BIBO) crystal with different phase matching directions,” Opt. Commun. **202**, 217 (2002).

[21] M. Ghotbi and M. Ebrahim-Zadeh, "990 mW average power, 52% efficient, high-repetition-rate picosecond-pulse generation in the blue with BiB_3O_6," Opt. Lett. **30**, 3395 (2005).

[22] M. Ghotbi, M. Ebrahim-Zadeh, A. Majchrowski, E. Michalski, I. V. Kityk,” High-average-power femtosecond pulse generation in the blue using BiB_3O_6”, Opt. Lett. **29**, 2530 (2004).

[23] A. Major, D. Sandkuijl, V. Barzda, "Efficient frequency doubling of a femtosecond Yb:KGW laser in a BiB_3O_6 crystal," Opt. Express **17**, 12039 (2009).

[24] A. C. Chiang, Y. C. Huang, Y. W. Fang, and Y. H. Chen, "Compact, 220-ps visible laser employing single-pass, cascaded frequency conversion in monolithic periodically poled lithium niobate," Opt. Lett. **26**, 66 (2001).

[25] G. D. Miller, R. G. Batchko, W. M. Tulloch, D. R. Weise, M. M. Fejer, and R. L. Byer,

"42%-efficient single-pass cw second-harmonic generation in periodically poled lithium niobate", Opt. Lett. **22**, 1834 (1997).

[26] S. Kurimura, N. Yu, Y. Nomura, "QPM wavelength convertersbased on stoichiometric lithium tantalate", in Advanced Solid-State Photonics (TOPS), Vol. **98** of OSA Trends in Optics and Photonics (Optical Society of America, 2005), paper 92 (2005).

[27] V. Pasiskevicius, S. Wang, J. A. Tellefsen, "Efficient Nd:YAG laser frequency doubling with periodically poled KTP", Appl. Opt. **37**, 7116 (1998).

[28] S. Forget, F. Balembois, G. Lucas-Leclin, "Picosecond laser source at 1 MHz with continuous tunability in the visible red band", Opt. Commun., **220**, 187 (2003).

[29] N. Pavel, I. Shoji, T. Taira, K. Mizuuchi, A. Morikawa, T. Sugita, and K. Yamamoto, "Room-temperature, continuous-wave 1-W green power by single-pass frequency doubling in a bulk periodically poled MgO:$LiNbO_3$ crystal" , Opt. Lett. **29**, 830 (2004).

[30] T. Suzudo, Y. Satoh, M. Hiroi, H. Mifune, Y. Sato, H. Ishizuki, T. Taira, O. Nakamura, S. Watanabe, and Y. Furukawa, "Advanced solid-state photonics", OSA Technical Digest Series (CD) (Optical Society of America, 2007), paper TuC3.

[31] M. Zhou, B. X. Yan, G. Bao, Y. Zhang, C. Gawith, D. D. Wang, Y. Qi, and Y. Bi, "52% optical-to-optical conversion efficiency in a compact 1.5 W 532 nm second harmonic generation laser with intracavity periodically-poled MgO:$LiNbO_3$", Laser Phys. 20, 1568 (2010).

[32] J. An, S. Zhao, G. Li, K. Yang, D. Li, J. Wang, M. Li, and Z. Zhuo," LD-pumped passively Q-switched Nd:YVO_4/YVO_4 green laser with a MgO-PPLN and Cr^{4+}:YAG saturable absorber", Laser Phys. Lett. **5**, 193 (2008).

[33] W. Koechner, M. Bass, "Solid-state lasers", Springer Science+Business Media, Inc., Sixth Revised and Updated Edition, (2006).

[34] W.P. Risk, "Compact blue-green lasers", Cambridge University Press, (2003).

[35] P. Banerjee, "Nonlinear optics theory, numerical modeling, and applications", University of Dayton, Dayton, Ohio, U.S.A. (2004).

[36] V. Wesemann, J. L'Huillier, L. Friess, "Optical properties of BiB3O6 with different phase matching orientations", Appl. Phys. B **84**, 453 (2006).

[37] J. Midwinter, J. Warner," The effects of phase matching method and of uniaxial crystal symmetry on the polar distribution of second-order non-linear optical polarization", Br. J. Appl. Phys. **16,** 1135 (1965).

[38] R. Hartke, "Intracavity frequency doubling of optically pumped semiconductor disk lasers to the green spectral range", PhD Dissertation, University of Hamburg, Germany (2008).

[39] J. A. Armstrong, N. Bloembergen, J. Ducuing, P. S. Pershan, "Interactions between light waves in a nonlinear dielectric", Phys. Rev. **127,** 1918 (1962).

[40] M. Fejer, G. Magel, D. Jundt, R. Byer, "Quasi-phase-matched second harmonic generation: Tuning and Tolerances", IEEE Journal of Quantum Electronics, **28,** 11 (1992).

[41] A. Ferguson, Department of Physics at the University of Strathclyde, Glasgow, Scotland, UK, http://phys.strath.ac.uk/12-370/ (2001).

[42] F. J. Kontur, I. Dajani, Y. Lu, and R. J. Knize, "Frequency-doubling of a CW fiber laser using PPKTP, PPMgSLT, and PPMgLN",Opt. Express **15**, 12882 (2007).

[43] A. Geng, Y. Bo, Y. Bi, "One hundred and twenty one W green laser generation from a diode-side-pumped Nd:YAG laser by use of a dual-V-shaped configuration", Optics and Lasers in Engineering **44,** 589 (2006).

[44] CASTON Inc., http://www.fz-caston.com (2010).

[45] New Rise Optics, http://www.newriseoptics.com

[46] Lithium niobate, http://en.wikipedia.org/wiki/Lithium_niobate (2011).

[47] L. E. Myers, W. R. Bosenberg, "Periodically poled lithium niobate and quasi-phase-matched optical parametric oscillators", IEEE J. Quantum Electron. **33**, 10 (1997)

[48] D. Jundt," Temperature-dependent Sellmeier equation for the Index of refraction, ne, in Congruent Lithium Niobate", Opt. let. **22**,1553 (1997).

[49] X. Zhang,"High-repetition-rate femtosecond optical parametric oscillators based on KTP and PPLN", PhD Dissertation, Marburg/Lahn, Germany 2002

[50] M. M. Fejer, G. A. Magel, D. H. Jundt, and R. L. Byer, "Quasi-phase-matched 1.064-um-pumped optical parametric oscillator in bulk periodically poled $LiNbO_3$" IEEE J. Quantum Electron. **28**, 2631 (1992).

[51] G. Miller, R. Batchko, W. Tulloch, "42%-efficient single-pass cw second-harmonic generation in periodically poled lithium niobate", Opt. Lett. **22**, 1834 (1997).

[52] H. Zhao, K. Sukhoy, T. Lima Jr., and A. Major, "Highly efficient, compact and Q-switched green microchip laser based on MgO-doped periodically poled lithium niobate", unpublished.